Requirements analysis and modelling of an antenna element for breast cancer microwave imaging.

Oleksandr Sergieiev

A thesis submitted to Auckland University of Technology in partial fulfilment of the requirements for the degree of Master of Engineering (ME)

2010

School of Engineering

Abstract

Malignant tumour diagnostics plays a significant role in the ability of contemporary medicine to treat cancer illnesses because early stage cancer can be treated successfully by well developed conventional techniques.

Microwave imaging is new and is still largely undergoing research. It exploits significant differences in the conductivity between malignant tumours and healthy breast tissue. One of the biggest challenges in such systems is a significant level of undesired signal reflections from the skin and fat layers, especially in the case of detecting small tumours.

One of the possible ways to overcome the current challenges in microwave imaging/detection is to use microwave holography and 3-D imaging. This method would involve an array of antennas and processing algorithms to reconstruct an image using the phase information of backscattered signal. The aim of the proposed research is to analyse the physical requirements for such a technique.

To formulate requirements for an antenna element antenna setup requirements have been considered. Such an approach let to address some of known issues related to human tissue properties and microwave propagation in it. From the other side quality of the reconstructed image would depend on the working frequency and placement of antenna elements. Thus the distribution of the antenna elements in the antenna array has been considered and the appropriate configuration proposed. The middle frequency was selected as trade-off between attenuation properties of the human tissue and desire to get best resolution. The antenna element design was selected on the base of the requirements.

Modelling of the antenna element was provided with open source software. Results of initial modelling were fairly close to the requirements. However performing several modifications with antenna dimensions and placement of the feeding point allow improving the model, particularly its reflection coefficient.

An eight of antenna elements were manufactured and measurements for the single and pair antenna element have been provided. This research has achieved its objectives successfully and identified areas for future development.

Table of Contents

List of Figures

List of Tables

Attestation of Authorship

‘I hereby declare that this submission is my own work and that, to the best of my knowledge and belief, it contains no material previously published or written by another person (except where explicitly defined in the acknowledgements), nor material which to a substantial extent has been submitted for the award of any other degree or diploma of a university or other institution of higher learning’

Oleksandr Sergieiev

February 2010

Acknowledgements

In completing this research I received help from a number of people. First I must thank my supervisor Dr Slava Kitaev for his support, guidance and advice during the course of this investigation.

I must also thank my friends and family for their support during the course of my research.

Finally, thank you to my wife Olga without whose love, support and infinite patience this thesis would not be possible.

Chapter 1 - INTRODUCTION

1.1 Motivation

According to the New Zealand Breast Cancer Foundation “Each year approximately 2,400 New Zealand women and approximately 20 men are diagnosed with breast cancer.” About 1 in 9 women will be diagnosed with breast cancer during their lifetime. In other countries the situation is not much better: in the United Kingdom, Europe and Australia the ratio is about 1 in 8 and in the United States the risk rises up to 1 in 7 (*NZ Breast Cancer Facts* 2008).

In New Zealand a special risk group consisting of Maori, Pacific and Asian women, who often avoid having regular screening mammograms. Mammography is a really unpleasant procedure and, unfortunately breast cancer is unpredictable. A woman may have many breast cancer risk factors, but not develop breast cancer. Likewise, a woman may be considered at low risk, but still develop breast cancer (*NZ Breast Cancer Facts* 2008) .

Breast cancer is the most common malignancy in women after skin cancer and the second leading cause of female cancer mortality (Fear, Hagness et al., 2002). Malignant tumour diagnostics plays a significant role in the ability of contemporary medicine to treat cancer illnesses. At the early stage cancer can be treated by well developed conventional techniques, but diagnostics is very often done too late and malignant tumours become too big and widely spread. Thus early diagnosis is the key to survival from breast cancer (Meaney et al., 2000).

The need for early stage cancer detection with high levels of specificity and sensitivity resulted in the active development of several diagnosis and treatment methods. Current detection methods include X-ray mammography – the standard method of breast imaging (Bond et al., 2003; Sill & Fear, 2005; L. Xu & Hagness, 2001). It produces an x-ray

image of a compressed breast. X-ray mammography exploits difference in the densities of the breast tissue, and it is sensitive enough to detect the most of lesions in the breast, but it misses up to 20 percent of lesions (Moore, 2001). It is difficult to gain an image from the 25% of women who have dense breasts. Usually, dense breasts are characteristic of women less than 40 years old, and it is one of the reasons why tumours are frequently detected in such women only when they are already large (Nunes & Schiabel, 2000). Often women find mammography uncomfortable and painful because this procedure requires pressing the breast between special plates. Moreover, regular and often illumination with an X-ray itself can cause cancer development.

1.2 Research Objectives and Contributions

The current screening method called mammography, which involves an X-ray imaging of a compressed breast, is unable to get reliable results for detecting treatable early-stage breast tumours (Bond et al., 2003; Sill & Fear, 2005; L. Xu & Hagness, 2001). Creating a tool for the reliable early detection of malignant tumour invasion would play significant role in ability of contemporary medicine to provide successful treatment for patients, due to timely medical intervention, and is a crucial factor for the survival and life quality of breast-cancer patients.

Current microwave imaging techniques, for example the ultra wide band (UWB) microwave radar technique, also have various weaknesses. For example, the UWB microwave exploits the impedance mismatch between normal and malignant breast tissue to detect, localize and characterize tumours based upon their radar cross section. Its accuracy depends upon the ability to model the effects of microwave propagation through the breast tissue. Most UWB microwave radar algorithms assume knowledge of certain patient specific characteristics, namely the location of the breast surface and the nominal dielectric properties of the breast tissue, in order to estimate the propagation effects (Winters et al., 2008). These

characteristics are mostly unknown *a priori* and may change significantly from patient to patient.

One of the possible new techniques for early stage breast cancer detection could be coherent beam forming and imaging the breast using an array of antennas and algorithms to reconstruct the image used phase information of the backscattered signal. The aim of the proposed research is to analyse the physical requirements for such a method, which includes suitable frequency band, polarization and irradiation levels. Due to high level requirements of this type of diagnostics and the special properties of breast tissue there are many unresolved problems which makes this research most suitable for the beginning stage of coherent microwave imaging development. Limitations of this possible approach would be the development of the antenna element and possible the construction for the antenna array for microwave imaging for early breast cancer diagnostics.

One of the possible ways to overcome the current challenges of microwave imaging/detection is to use an interferometer. This method would involve an array of antennas and processing algorithms to reconstruct an image.

An interferometer is used in radio astronomy (Taylor, 2007). Especially attractive with this method are the recent advances in digital signal processing techniques which have become widely available at a lower cost. The most similar counterpart of developed technique is early stage breast cancer detection using indirect microwave holography developed by(Elsdon et al., 2007).

Proposed method of the coherent beam forming for medical microwave imaging implies special requirements for suitable antenna elements. The original contribution of the current research is the analysis of requirements and the modelling of suitable antenna element.

1.3 Organization of the Thesis

The rest of the thesis is organized as follows:

Chapter Two provides the related background knowledge and the current methods of microwave breast cancer detection. In this chapter, properties of human tissue in the microwave range are revealed and the breast tissue model is discussed.

In Chapter Three, a brief review of principles for implementation 3-D Holography in general and in terms of microwave imaging for medical purposes is given. Key issues such as requirements for the antenna setup, relationship between frequency and resolution of the imaging system, role of the inner propagation media of the antenna setup are considered. Suitable antenna setup construction is proposed and possible antenna distribution in the array discussed.

In Chapter Four the requirements for the antenna element and the antenna array are given. The middle frequency for the developing antenna element is selected. The selection of the polarization type is discussed. The issue of the mutual coupling in the antenna array is considered.

In Chapter Five, after a brief explanation of the design flow and methodology, the selection of the modelling tool is discussed. Then the selection of the basic antenna design is represented. Modelling and optimization of the antenna element are considered and a compact patch antenna for given requirements is developed and its characteristics are studied.

In Chapter Six the measurement results for a single Antenna element and coupling of two antennas are represented.

In Chapter Seven the discussion of results of modelling and measurements of the antenna element is provided. Particular issues related to the modelling and production technique are discussed together with the quality of the media used in the measurements. Some possible ways to overcome any encountered difficulties are discussed.

Chapter Eight provides overall conclusion for the current work.

Chapter 2 - Background and Literature review

2.1 State of the Art

2.1.1 Current breast imaging techniques

The current gold standard for breast cancer detection is X-ray mammography. Ultrasound techniques as well as microwave radiometry can be considered as supplementary to mammography. Magnetic Resonance Imaging (MRI) is the most reliable though the most expensive contemporary technique for breast cancer detection. These techniques are considered in more detail in the current Chapter.

X-ray mammography is the most widely used technique for breast cancer detection and imaging. It produces an X-ray image of a compressed breast (Figure 2.1). X-ray mammography exploits the differences in the densities of the breast tissue, and it is sensitive enough to the detect most of the lesions, but still misses up to 20 percent of lesions (Moore, 2001). .

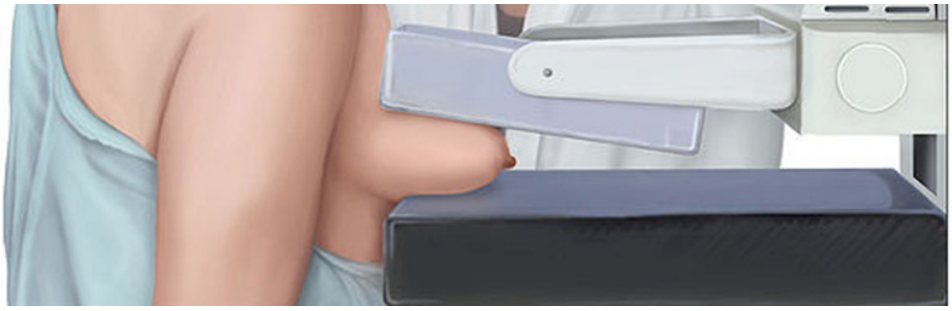

Figure 2.1 X-ray mammography - standard method of breast imaging. It produced an x-ray image of a compressed breast[1].

If there is no concern about the inconveniences for patients and the possible threat to health from the accumulating low-dose ionizing radiation over repeated scans, the X-ray mammography still does not provide reliable diagnostic results because after 10 mammograms the estimated cumulative risk of a false positive result is 49.1 percent (95 percent confidence interval, 40.3 to 64.1 percent) and 22.3 percent (95 percent

[1] Hoofring, A. (2007). Fragment from the figure "Mammography in process". Retrieved 12.11.2009, from http://en.wikipedia.org/wiki/Mammography

confidence interval, 19.2 to 27.5 percent) after 10 clinical breast examinations (Elmore et al., 1998) while 4%–34% of all breast cancers are missed by conventional mammography (Huynh et al., 1998)

In some cases ultrasound is used clinically to determine whether a lesion detected on a mammogram is a liquid cyst or a solid tumour. However, the investigations conducted by (Wendie et al., 2008) have demonstrated that while adding a single screening ultrasound to mammography will yield an additional 1.1 to 7.2 cancers per 1000 high-risk women, it also substantially increases the number of false positives.

MRI is the only contemporary method which gives high accuracy and is reliable for small malignant tumour detection, but this method is still too expensive and results can be delayed. For this reasons an MRI is not available to a wide population even in the richest countries.

Microwave radiometry is a relatively new addition to breast cancer detection. It measures microwave emissions to detect the presence or absence of abnormal thermal activity in the breasts, which could reduce non-cancerous breast biopsies based on mammographic false positive results.

2.1.2 **Microwave breast imaging**

Microwave imaging exploits significant differences in the conductivity between a malignant tumour and healthy breast tissue. Normal breast tissue is more transparent to microwaves because malignant tissue contains more water and blood. The area of bordering tissue has a high contrast in dielectric properties, therefore some of the energy of a microwave signal propagating through the tissue gets reflected back. Such reflected and backscattered signal can be detected and examined.

Dielectric properties of biological tissues at radio and microwave frequencies have been the subject of research by many groups and comprehensive surveys have been published (C. Gabriel et al., 1996;

Gabriel et al., 1986; Gabriel & Peyman, 2006) and could be used as a base point to evaluate the behaviour of microwaves in human's tissue.

Several microwave imaging concepts have recently been developed for breast cancer detection, such as Microwave-Acoustic Imaging (Chunjing et al., 2006; Kruger et al., 1999; M. Xu & Wang, 2002), Passive Microwave Imaging (Bocquet et al., 1990; K. L. Carr, 1989), Hybrid Tomography Imaging and Ultra Wideband Radar systems (Fear, Hagness et al., 2002; Fear, Li et al., 2002; Meaney et al., 1999). One of the biggest challenges for developers of these systems, especially in detecting small tumours, is a significant level of undesired signal reflections from the skin and fat layers. These are due to considerably different dielectric properties and a large reflection surface.

Microwave imaging has been used in various application areas. This thesis will discuss passive, active and hybrid approaches to microwave imaging methods for breast cancer detection.

The measuring of temperature differences between malignant and normal breast tissue is passive microwave radiometry (Kenneth L. Carr, 1989).

Active microwave imaging exploits the significant dielectric contrast between malignant tumours and normal breast tissue, which results in microwave scattering or selective heating/absorption (Arunachalam, 2007; S. K. Davis et al., 2008; Fear, Hagness et al., 2002; Li et al., 2004; P. M. Meaney et al., 1995). Active microwave imaging exploits non-ionizing electromagnetic waves, and does not require breast compression between special plates. The radiated power level is much lower than that of a conventional mobile phone. Due to a much longer wave length, direct microwave imaging does not provide the same spatial resolution as X-rays, but it has the potential to offer improved sensitivity and resolution with computational approaches relaying on the high dielectric contrast, which is usually greater than 2 : 1 (C. Gabriel et al., 1996; S. Gabriel et al., 1996a, 1996b), and much higher than the contrast in radiographic density exploited by X-ray mammography - only several percents.

Under the hybrid microwave-induced acoustic imaging, the breast is irradiated by microwave signals, which are transmitted into breast to heat tumours, and ultrasound transducers detect pressure waves are generated by tumour expansion. The received waveforms are used to infer the distribution of tissue dielectric-properties inside of the breast.

2.1.2.1 Passive techniques

The passive techniques are based on measuring temperature using radiometers and creating a temperature map (Bocquet et al., 1990; K. L. Carr, 1989). Because breast tissue is more translucent to microwaves than IR signals, microwave systems offer an advantage over infrared. The main principle is based on increased tumour temperature comparative to healthy breast tissue. There are quite a few examples of microwave radiometry systems for breast cancer detection (Bocquet et al., 1990; Carr et al., 2000; Hartov et al., 2000)

Reconstructed images display the temperature measured over a quadrant of the breast. For diagnosis, images of the suspicious lesion and corresponding area on the other breast are compared. Clinical results obtained with the ONCOSCAN^{TM} (Carr et al., 2000) suggest that microwave radiometry has the potential to assist in the diagnosis of suspicious areas on mammograms.

2.1.2.2 Active microwave imaging techniques

There are three types of active microwave breast imaging techniques currently being developed: microwave tomography (Bulyshev et al., 2001; Liu et al., 2002; Meaney et al., 2000; Meaney et al., 1999; Souvorov et al., 2000), UWB microwave radar techniques (Bond, Li, Hagness, & Van Veen, 2003; Fear, Li et al., 2002; Fear & Stuchly, 2000; Hagness, Taflove, & Bridges, 1998a, 1999; L. Xu & Hagness, 2001), and hybrid microwave-induced acoustic imaging (Kruger et al., 1999; Tao et al., 2007; Wang et al., 1999).

The microwave tomography recovers the spatial distribution of dielectric properties in the breast by solving non-linear inverse scattering problems to create a reconstruction.

Early experimental systems for microwave tomography have used single pair transmit/receive antenna, or even one antenna element for raw data acquisition, and so called Synthetic Antenna Array have been created by mechanical relocations of antennas. Contemporary microwave tomography uses antenna arrays that significantly decrease the required time for raw data acquisition which in turn addresses the problem of possible patient motion. Moreover, a fast electronically scanned microwave array provides the ability of dynamic imaging and thus functional studies which in turn may bring new information to the diagnosis and therapy. Conversely in electronically scanned microwave arrays, which typically consist of multiple transmit/receive elements in close proximity, a problem emerges which is associated with the undesirable coupling of the imaging transceiver elements to the surrounding environment which degrades the imaging performance. Taking into account possible features of the microwave imaging methods for the electromagnetic properties of tissue, it is obvious that many research groups are actively working on the development of related techniques (J. Ch Bolomey et al., 1991; Bulyshev et al., 2001; Jofre et al., 1990; P. M. Meaney et al., 1995; Miyakawa, 1993; Semenov et al., 2005; Semenov et al., 1996; Semenov et al., 2002).

There are three approaches that have been discussed in the literature for dealing with the coupling issue.

The first and most obvious way is to decrease antenna interactions by using improved hardware implementations to get fast and accurate antenna relocation. Actually this one has been used from the very beginning in systems with a single transmitter and single receiver that use mechanical motion to obtain enough data for image reconstruction. Unfortunately, it is too difficult to develop a suitable mechanical positioning system with data acquisition time, comparative to data acquisition times for systems with an electronically scanned microwave array. Special sophisticated modulation methods have been employed to isolate the measured response from neighbouring sensors within an array in

multisensory technologies (Bolomey Ch et al., 1982; J. C. Bolomey et al., 1983) and other approaches that remain in active use (Franchois et al., 1998).

Secondly, a strategy is to use a prior calibrating process in order to minimize the undesirable environmental coupling effects and improve the quality of image reconstruction. There are examples (Franchois et al., 1998) and (Meaney et al., 1998), where calibration methods that operate on the raw measurement data prior to image reconstruction can provide some improvements. Also the calibration may significantly improve the performance of single transmit/receive as well as array systems. The essence of this method consists of subtraction of the perturbations in the measured data by incorporating certain types of model fits to measurements, obtained under homogeneous conditions, which are intended to eliminate offsets in individual antenna elements or data acquisition channels. On the other hand it may be possible to implement calibration which can change the measured data itself.

The third approach is to take into account the model of the imaging system array in the image reconstruction algorithm for antenna array to eliminate undesirable coupling from measured data. This strategy is used in the near-field model-based image reconstruction context (Caorsi et al., 1995; Caorsi et al., 1993; Franchois & Pichot, 1997; Paul M. Meaney et al., 1995). In essence this approach is a computing of the electric fields with the underlying computational model in comparison to measured values. An electric field integral equation method was reported (Franza et al., 2002), where the problem space occupied by the imaging system sensors was explicitly modelled, in addition to the traditional target region domain. This provides a means of representing both the geometry and electrical composition of the sensor array and has been investigated in both two and three dimensions. This successfully eliminates tangential components of the total electric field on the antenna surface especially in the case of a metallic antenna. It is obvious that the most successful result can be achieved by a combination all of these techniques.

The UWB radar approaches seek only to identify the presence and location of significant backscattered energy from malignant breast tumours. However, the computational method representative of the class of UWB radar techniques for microwave imaging via space–time (MIST) beam forming was recently proposed (Bond et al., 2003; S. K. Davis et al., 2003). With this method each antenna in an array transmits a low-power UWB signal sequentially into the breast and records the backscatter signal. The beam former is designed to image backscattered energy as a function of location in the breast and use recorded backscatter signals as raw data. Due to a significant dielectric contrast with normal breast tissue, malignant tumours produce localized regions of backscatter energy, which are reconstructed in the image. The detection of abnormalities inside of the breast is the main scope of this approach. The examination of other scattering characteristics such as polarization and spectral signatures has to be involved to provide a differentiation between malignant and benign tumours (Hagness et al., 1999).

UWB radar techniques based on simple focusing schemes (Fear, Li et al., 2002; Fear & Stuchly, 2000; Hagness et al., 1998b; L. Xu & Hagness, 2001) were significantly improved by the MIST beam forming approach. The theoretical feasibility of two-dimensional (2-D) space–time beam formers for tumour detection was demonstrated by (Bond et al., 2003; S. K. Davis et al., 2003). Taking into account a number of potential challenges associated with the imaging of heterogeneous breast tissue one can say that MIST beam forming has also demonstrated good robustness.

The UWB radar techniques in general are younger then microwave tomography. An extensive experimental results have been obtained using a pre-clinical prototype of a microwave tomography system (Meaney et al., 2000), while only a very preliminary experimental studies have been reported to date using the UWB radar. Some experimental feasibility studies (Fear, Sill et al., 2003), quite simple time-shift-and-sum focusing schemes (Fear, Li et al., 2002; Fear & Stuchly, 2000; Hagness et al.,

1998b; L. Xu & Hagness, 2001) were used to create 2-D images. In those approaches the hollow PVC pipe in free space represented skin and normal breast while the wood, copper, or water-filled object represented a malignant tumour. In a more recent study, the pipe was illuminated by a large horn antenna or resistively loaded monopole antenna positioned at several points. The study was designed to simulate the system configuration with the patient lying in a prone position with antennas surrounding the breast. Small water-based synthetic malignant tumours were imaged in a homogeneous 3-D background in the initial experimental feasibility study of the MIST beam forming approach (Li et al., 2002). During this simulation, dielectric contrast between the normal and malignant-tissue simulator was larger than really measured in the actual breast tissue and the provided phantom did not contain a layer of skin.

2.1.2.3 Hybrid microwave imaging techniques

The hybrid technology represented by microwave-induced thermo acoustic tomography (MITT) uses the advantages of ultrasonic and microwave imaging techniques. While other computed tomography modalities are based on a direct physical effect, the MITT is based on the compound of biological physical effects. As shown in the definition the measuring item for the MITT is ultrasonic wave that have been induced, in the biological tissue which was irradiated by the microwave. It provides the advantages of easy realization and improved spatial resolution as well as a high contrast and safe imaging mode. It has been suggested by many researches that thermo acoustic tomography using either pulsed radio frequency (RF) or pulsed laser can be a powerful imaging technology with good spatial resolution (Kruger et al., 2002; Wang et al., 1999; M. Xu et al., 2003).

The different heat absorption rate due to the conductivity contrast between malignant and normal human tissue is what MITT is based on. Pulse electromagnetic energy which causes the thermo elastic expansion is absorbed by tissues when biological tissues are irradiated by microwave pulses. The thermo elastic expansion induces the acoustic waves which

carry information about the radio frequency absorption or initial pressure due to differences in thermo and acoustic properties between malignant and normal tissues in the microwave radio frequency spectral range.

The penetration depth, ratio of absorption, velocity and efficiency of thermal conversion, and the utilization ratio of thermal acoustic information is directly related to the microwave source and the setting of the source parameter. Thus the initial choice of these parameters is one of the critical factors for appropriate data collection. In the initial study of the thermo acoustic tomography development the microwave source with a single frequency was used to induce biological tissues (Wang et al., 1999; M. Xu & Wang, 2002, 2003). The human body consists of different biological tissues, most of them are not homogeneous mediums with different electromagnetic parameters and thus a biological tissue is a very complex electromagnetic system. Obviously different imaging results will be obtained with different microwave frequencies irradiating the tissues of human body. Some authors claim that the wider the band used, the richer the information is (Chunjing et al., 2006). Others supposed that electromagnetic fields in the RF range of 300 to 3000 MHz are the most useful in the study of soft tissues sized in centimetres (M. Xu & Wang, 2002). This frequency range is wide enough and the RF penetration depth varies depending on the RF frequency itself as well as on the tissue properties. It is obvious that a higher frequency can obtain higher spatial resolution, but the higher frequency in tissues leads to the attenuation of the microwave signal and has lower penetration depth. High bandwidth is required in SAR and hybrid methods to meet sufficient imaging resolution demands. Such a signal can be carried by using a high frequency microwave (Chunjing et al., 2006; Shakti K. Davis, 2006). On the other hand, detected signal with a low frequency has better penetration depth because of the heavy loss during the high frequency electromagnetic wave propagating in the biological tissues. It is one of the main issues to select the appropriate frequency to satisfy both the penetration depth in biological tissue and high resolution in the tissue simultaneously. It is why MITT developers select an adaptive irradiation frequency in order to

balance the penetration depth and the resolution. Other research groups have used a special step frequency under a different frequency in a range of set wavebands to carry the signal through the biological tissues for microwave imaging, but solving complex nonlinear equations must be used in this method (Converse et al., 2006).

2.2 Problem definition

In microwave imaging using the method of coherent beam forming, the biological tissues should be illuminated by the microwave source and backscattered energy will be collected by multiple antennas. Phase information from detected signals will be used later for image reconstruction. In Chapter 3, a more detailed introduction of the proposed method will be given. It is well-known that high frequency electromagnetic waves energy will be attenuated in a loss media like human tissue. The attenuation level depends on the frequency and a higher frequency corresponds to higher attenuation (Duck, 1990). On the other hand the resolution of the developed technique directly depends on wave length. The shorter is the wave length - the better is the resolution. We can increase the power of the illumination signal but we are going to illuminate human breast tissue and power dissipated in the tissue will heat it up. Whereas for some applications, or the mentioned above hybrid techniques this is the goal, in our case this dissipation is undesirable. Thus we have to find a trade-off between a desirable resolution and the undesirable dissipation of high frequency power by selecting an appropriate frequency as well as other characteristics of the developing antenna element.

2.3 Breast Tissue Dielectric Model

In the proposed method a difference in relative permittivity of the malignant tumour and healthy breast tissue for early breast cancer detection is exploited. The challenge is that a human breast has inhomogeneous structure and related microwave distortions as well as attenuation of the signal in the microwave frequency band will appear.

Therefore understanding the physiological structure and morphology of breast and related electrical properties of both normal and cancerous breast tissue needs to be considered and understood.

2.3.1 Physiological structure of breast

The physiological structure of the human breast is the subject of numerous researches. As can be seen on Figure 2.2 a breast resides on the chest muscles that cover the ribs. Each breast is made of 15 to 20 lobes. Lobes contain many smaller lobules. Lobules contain groups of tiny glands that can produce milk. Milk flows from the lobules through thin tubes called ducts to the nipple. The nipple is in the centre of a dark area of skin called the areola. Fat fills the spaces between the lobules and ducts.

The breasts also contain lymph vessels. These vessels lead to small, round organs called lymph nodes. Groups of lymph nodes are near the breast in the axilla (underarm), above the collarbone, in the chest behind the breastbone, and in many other parts of the body. The lymph nodes trap bacteria, cancer cells, or other harmful substances. (*The Breasts*, 2008)

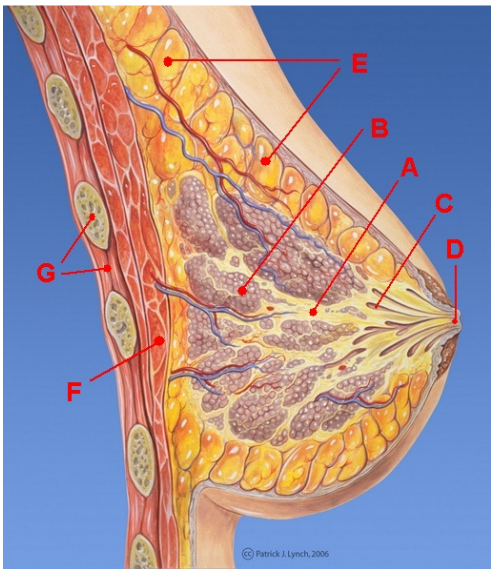

Figure 2.2 Normal breast structure. Figure adopted from Wikipedia. Originally retrieved 21.02.2009, from http://en.wikipedia.org/wiki/File:Breast_anatomy_normal.jpg.

Breast profile[2]:

A. ducts
B. lobules
C. dilated section of duct to hold milk
D. nipple
E. fat
F. pectorals major muscle
G. chest wall/rib cage

2.3.2 **Dielectric properties of breast tissue**

More than a century ago investigators became interested in the bulk electrical properties of tissues and blood (Hermann, 1872). They discovered that the electrical properties of such materials differ greatly from those of simple electrolyte solutions. They observed, for example, that upon the application of a direct current (DC) potential step, the current changes with time, beginning with a charging spike. They also observed the hysteresis phenomena. These effects were understood poorly for some time, and in retrospect the data might be suspected of being

[2] Lobular Carcinoma in situ (LCIS). (2009). Retrieved 30.10.2009, from http://www.breastcancer.org/pictures/types/dcis/lcis.jsp

influenced by electrode polarization artefacts. This early work led to the concept of tissue “polarization” (Foster & Schwan, 1996).

In 1872 Hermann reported that the DC resistance of muscle varies by a factor of 4 to 9 with orientation in freshly excised tissue, but this anisotropy slowly disappears after death. He interpreted this as arising from the microscopic structure of the tissue, but incorrectly proposed that it arose from different ionic permeability in directions perpendicular and parallel to the fibers. Hermann was one of the first who have measured the resistance of tissues to “alternating” currents (AC) using an apparatus of his own construction that alternately applied current pulses of opposite signs to the tissue (Foster & Schwan, 1989).

A large number of studies have been carried out since the beginning of the 20th century, characterizing the dispersive dielectric properties of biological tissues at frequencies ranging from DC to hundreds of GHz. These results have been extensively reviewed and tabulated by various authors (Cole & Cole, 1941; C. Gabriel et al., 1996; S. Gabriel et al., 1996a, 1996b; Johnson & Guy, 1972).

2.3.2.1 Brief Overview of Dielectrics and Their Properties

The charge and current densities induced in response to an applied electric field of unit amplitude are determined by the dielectric permittivity ε and conductivity σ of a material. To illustrate these definitions let’s see the example of an idealized parallel-plate capacitor, of two plates area A and separation d, which contains the material under investigation with relative permittivity ε and conductivity σ Figure 2.3. Initially, let the region between the plates be a vacuum.

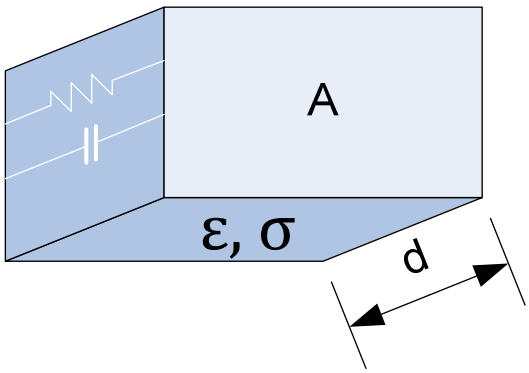

Figure 2.3 Idealized parallel-plate capacitor, of two plates area A and separation d, which contains the material under investigation with relative permittivity ε and conductivity σ between plates. Figure adopted from (Foster & Schwan, 1989).

A constant voltage difference V between the plates will induce a charge density D given by (Foster & Schwan, 1989)

$$D = \varepsilon_0 E = \frac{\varepsilon_0 V}{d} \tag{2.1}$$

Where: E is electric field

and ε_0 is permittivity of free space (8.85×10^{12} F/m)

For simplicity let's start with a plain wave in a lossless non-magnetic medium. Velocity and corresponding wavelength are different from those in free space

$$v = \frac{c}{\sqrt{\varepsilon_r}} \tag{2.2}$$

Where: c is velocity of light in free space

and ε_r is static relative permittivity

The static relative permittivity of a medium is defined as

$$\varepsilon_r = 1 + \chi_e \tag{2.3}$$

Where: χ_e is static electric susceptibility, a measure of how easily it polarizes in response to an electric field

Then wavelength in medium:

$$\lambda = \frac{\lambda_0}{\sqrt{\varepsilon_r}} \tag{2.4}$$

Where: λ_0 is the free space wavelength

Relative permittivity ε_r is always greater than or equal to one. Thus a wave travelling in a dielectric has a lower velocity and shorter wavelength than in free space. Obviously the velocity and wavelength will be different when the wave travels in different materials.

The propagation direction usually changes when a wave is incident at the interface between regions composed of two different materials. A wave is partially reflected from the interface and partially transmitted from one region into the other. The reflection and transmission are determined by the intrinsic impedance contrast of two different materials.

The intrinsic impedance is a property of the dielectric material. It is defined as the square root of the ratio of the magnetic permeability to the permittivity:

$$Z = \sqrt{\frac{\mu}{\varepsilon}} = \sqrt{\frac{\mu_r \mu_0}{\varepsilon_r \varepsilon_0}} \tag{2.5}$$

Where: μ_0 permeability of free space

and μ_r is the ratio of the permeability of a specific medium to the permeability of free space

For a non-magnetic dielectric where μ_r = 1, the intrinsic impedance in the dielectric depends on permittivity and is related to the intrinsic impedance of free space as:

$$Z = \sqrt{\frac{\mu_0}{\varepsilon_0}}\sqrt{\frac{1}{\varepsilon_r}} \tag{2.6}$$

Where $\sqrt{\frac{\mu_0}{\varepsilon_0}} = 377\ \Omega$ is intrinsic impedance of free space.

The reflection coefficient Γ is the ratio of the amplitudes of the reflected and incident electric fields used to describe the wave reflection (Hayt & Buck, 2001). When a uniform plane wave is normally incident on the planar boundary, the reflection coefficient is:

$$\Gamma = \frac{Z_1 - Z_2}{Z_1 + Z_2} \tag{2.7}$$

Where: Z_1 is the intrinsic impedance of material 1

and Z_2 is the intrinsic impedance of material 2

Considering the definition of the intrinsic impedance equation (2.6) one can develop (2.7) as:

$$\Gamma = \frac{Z_1 - Z_2}{Z_1 + Z_2} = 1 - \frac{2Z_1}{Z_1 + Z_2} = 1 - \frac{2}{1 + \sqrt{\frac{\varepsilon_1}{\varepsilon_2}}} \tag{2.8}$$

Hence, the reflection coefficient is determined by the contrast in the dielectric properties of the two media.

The transmission coefficient T is also determined by intrinsic impedance as:

$$T = \frac{2Z_2}{Z_1 + Z_2} = 1 + \Gamma \tag{2.9}$$

As will be shown below, in the female breast a malignant tumour has higher dielectric property values than normal fatty tissue. The significant contrast results in microwave reflections from the interface between these two different tissues. Active microwave breast cancer detection techniques are based on this electrical difference.

2.3.2.2 Properties of human tissue

The human breast like other biological material is a mixture of water, ions, and organic molecules organized in cells, sub-cellular structures, and membranes, and its dielectric properties are highly frequency dependent in the range from Hz to GHz. The spectrum is characterized by three main dispersion regions referred to as alpha, beta, and gamma regions at low, intermediate, and high frequencies (C. Gabriel et al., 1996). Each of these regions is, in its simplest form, the manifestation of a dominant polarization mechanism.

For the purposes of microwave imaging using the method of coherent beam forming, biological tissues can be classified as high water-content and low water-content, since the water content dominates the tissue dielectric properties at these frequencies. High water-content tissue consists of approximately 60-80% of water, including muscle and skin. Low water-content tissue includes bone and adipose tissue consisting of approximately 40% and 10% water respectively (Duck, 1990; Foster & Schwan, 1989). Dielectric properties of some tissues exhibit significant variations depending on their structure and precise measurement location. For example, depending on whether the measurement field is oriented parallel or transverse to the muscle fibers. Therefore the dielectric properties of muscles are anisotropic.

A good understanding of the dielectric properties of malignant and healthy tissues is important for the development of diagnostic and therapeutic technologies that utilize the microwave frequency range. It have been shown that dielectric properties of malignant tissues differ from normal tissues by varying amounts, depending on the specific tissue type (Fear, Hagness et al., 2002; Hagness et al., 1998a). Any dielectric-properties at

these frequencies are likely to be different due to variations in water content between normal and malignant tissues. Generally malignant tumours develop an extensive network of blood vessels to aid their growth, resulting in increased water content in the region of the malignant tumour.

Keeping in mind that the variation of conductivity and permittivity of the human tissue with frequency is mutually dependent, we should consider the conductivity of tissues separately from their permittivity. Normally conductivity of tissues increases while frequency arises, mostly from Maxwell-Wagner effects (Wagner, 1914) and can be interpreted as a progressive increase in the volume fraction of the suspension that is accessible to the applied current. At low frequencies, and for most practical purposes, only their conductivity can be taken into account. We can consider several frequency regions, using each of the Maxwell-Wagner theory, which can be applied to the data from tissues with a different volume fraction of the tissue being excluded from the current flow (Foster & Schwan, 1989).

There are three effects which add significantly to the conductivity at these frequencies:

- A Maxwell-Wagner effect due to interfacial polarization of tissue solids through the tissue electrolyte
- Dielectric loss of small polar molecules and polar side chains on proteins
- Dielectric relaxation of water

As was mentioned above, a monotonic decrease in permittivity is associated with the monotonic increase in conductivity with frequency. There are three major dispersion regions, the alpha, beta, and gamma dispersions, with dielectric increments. The corresponding relaxation frequencies are in the ranges of kilohertz, hundreds of kilohertz, and gigahertz. However, the alpha and beta dispersion regions typically show

a broad distribution of relaxation times, and some overlap of these regions is typically observed in tissues.

The alpha dispersion is manifested by the very large increase in permittivity at frequencies of kilohertz. Ionic diffusion processes lead to large permittivity increases at such frequencies in objects of micron and larger sizes, and no doubt these effects occur in tissues as well.

The beta dispersion occurs at radiofrequencies and arises principally from the capacitive charging of cellular membranes in tissues. In addition, a smaller component might arise at high radiofrequencies from dipolar orientation of tissue protein.

Most interesting for us is the microwave frequency range. The gamma dispersion occurs with a centre frequency near 25 GHz at body temperature, due to the dipolar relaxation of the water that accounts for 80% of the volume of most soft tissues.

In addition to the three major dispersion regions mentioned above, tissues and other biological materials typically exhibit a small dispersion between 0.1 and 3 GHz, which several authors have called the delta dispersion (Foster & Schwan, 1989).

As the waves penetrate into the tissues the absorption of microwave power will result in a progressive reduction of wave power density. As it stated in the (Johnson & Guy, 1972), we can quantify this by defining a depth of penetration or a distance that the propagating wave will travel before the power density decreases by a factor of $\sqrt{e}$. The absorption or heating patterns of the biological system induced by radiation will not be uniform and dependent on the dielectric properties of the tissues. In tissues with high water content such as muscle, brain tissue, internal organs, and skin the absorption is high and the depth of penetration is low, while the absorption is an order of magnitude lower in tissues of low water content, such as fat and bone. Reflections between tissues of high and low water content can produce severe standing waves accompanied by “hot spots” that can

be maximum in either tissue, regardless of dielectric constant or conductivity.

The normal breast largely consists of adipose tissue, and the presence of infiltrating neoplastic tissues of high water content will certainly lead to pronounced changes in the dielectric properties of breast tissue. As early as 1926, Fricke and Morse made measurements of normal and malignant breast tumours and reported that the permittivity of neoplastic breast tissues at 20 kHz was higher than that of non-malignant tumour and normal breast tissues, and suggested the feasibility of diagnosis based on this difference(Foster & Schwan, 1996). Fat cells are filled with lipid, and thus have lower water content than other tissues. At microwave frequencies, this results in lower permittivity and conductivity, as these quantities increase with water content. This also suggests the existence of a large contrast between high water content tumours and low water content normal breast tissue. Benign tumours consist primarily of fibrous tissue and ducts, and are likely to have different properties from the high water content malignancies.

It was shown that the dielectric properties of breast tissue are primarily determined by the adipose content. The most recent studies of breast tissue show that secondary factors such as patient age, tissue temperature and time between excision and measurement had only negligible effects on the observed dielectric properties. Finally, there is no statistically significant difference between the within-patient and between-patient variability in the dielectric constant and effective conductivity (Lazebnik et al., 2007). This heterogeneity in the dielectric properties of normal breast tissue needs to be taken into account as well.

2.4 Summary

In this chapter the breast tissue dielectric model has been discussed. An overview of static fields and electromagnetic waves in dielectric has been presented. Properties of the human tissue vital for microwave holography

such us conductivity, permittivity and related depth of penetration have been considered.

Ongoing requirement analysis is based on the materials considered in this chapter.

Chapter 3 - Microwave Imaging and 3-D Holography

3.1 Introduction

In this chapter, a short review of microwave Imaging and 3-D Holography will be given, and then the antenna setup requirements analysis, interferometry method and dependency between frequency and resolution with propagation media properties will be introduced. Possible antenna setup constructions and the requirements for the antenna element distributions in the array will be discussed. Far target of the current job is 3-D microwave imaging, thus both optical holography and radio interferometry will be considered.

3.2 Holography and radio interferometer

The method of imaging by reconstructed wave-fronts and the terms holograms and holography were invented by Dennis Gabor in 1947 (Gabor, 1948). The theory of holography was developed by Dennis Gabor, a Hungarian physicist. The word hologram is derived from the Greek words "holos" meaning whole or complete and "gram" meaning message. His theory was originally intended to increase the resolving power of electron microscopes. Gabor proved his theory not with an electron beam, but with a light beam. The result was the first hologram ever made.

As mentioned above in classical realization optical holography included two phases and requires a coherent light source. In an attempt to improve the resolving power of the electron microscope, Gabor' proposed a two-step method of optical imagery. In the first step an object is illuminated with a coherent electron wave or a coherent light wave. The object is assumed to be such that a considerable part of the wave penetrates undisturbed through it. A diffraction pattern, called a hologram, which is formed by the interference of the secondary wave arising from the presence of the object with the strong background wave, is recorded on a photographic plate. If the plate, suitably processed, is replaced in the

original position and is illuminated by the background wave alone, the wave is transformed by the plate containing the information about the original object, and an image can be extracted from the photograph by optical processes. In order to 'reconstruct' the object from this 'substitute' wave, it is only necessary to send it through a suitable image-forming system, and an image will appear in the plane conjugate to the plane in which the object was situated. We shall only be concerned with the optical principle involved (Born & Wolf, 1999).

The hologram diffracts two waves, one proportional to the object-scattered field and another proportional to its complex conjugate. Both waves form images, but they can overlap and obscure each other. This overlap was a disadvantage to holography for several years until Leith and Upatneiks introduced a new experimental technique; since then, holography has grown rapidly (Tricoles & Farhat, 1977).

A coherent light source was one of the biggest challenges for holography development. Another problem is the fact that there are no materials available at the moment which can evaluate the phase or direction of light, only intensity (Benton & Bove, 2008). Thus to get phase information it is necessary to use a coherent reference wave. In practice, that means that they both have to come from the same laser. On the plane where they overlap, a characteristic “picket fence-like” interference pattern is formed which is imprinted on the film. The larger the angular difference between the beams, the finer the pattern becomes (Benton & Bove, 2008). It is very similar to the example that will be explained below. In our case of microwave holography we have to use antennas for intensity measurements thus the proper placement of antenna elements becomes critical, which will be discussed in the section 3.7.

The positive side of microwave holography is that we can achieve the required coherence and phase control with considerable ease. Thus the main issues are the wave length, number and the distribution of measured points (to read antenna elements). Practical solution of later problem is beyond the scope of current research. Thus, we will concentrate our

efforts mostly on the frequency, polarization of incident microwaves and coupling between antennas in our setup.

As mentioned above, interferometry is the technique of examining the properties of two or more coherent waves by studying the pattern of interference created by their superposition. Let's consider two element elementary interferometer responses in accordance to geometry shown in Figure 3.1. Electromagnetic wave "W" arrives to antennas A1 and A2. Let us assume that it is a monochrome plane wave with frequency f. Antennas A1 and A2 are separated by the distance D, called the baseline.

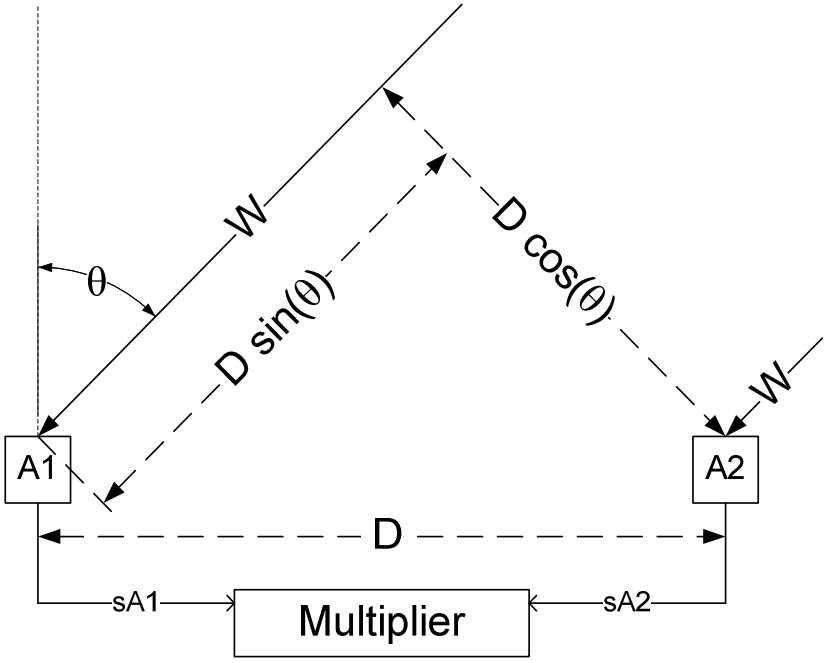

Figure 3.1 Elementary interferometer. Two antennas "A1" and "A2" separated by the distance "D". Plane wave "W" arrives from the direction deflected from normal to separation distance by angle "θ". Signals "sA1" and "sA2" are mutually multiplied. Figure adopted from (Thompson, 2007).

The wave front from the source in direction θ arrives to the right-hand antenna before it reaches the left-hand. Time difference τ_g should be determined as:

$$\tau_g = \frac{D}{v} sin\,(\theta) \tag{3.1}$$

Where: D is separation distance between

v is velocity of the arrived wave front

and θ is deflection angle from normal to separation distance

On the exit of multiplier should be a signal proportional to

$$\begin{aligned} F &= 2\,sin(2\pi ft)\,sin\left(2\pi f\left(t-\tau_g\right)\right) \\ &= cos\left(2\pi f\tau_g\right) - cos(4\pi ft)\,cos\left(2\pi f\tau_g\right) \\ &\qquad - sin(4\pi ft)\,sin\left(2\pi f\tau_g\right) \end{aligned} \tag{3.2}$$

Where: f is temporal frequency of the receiving signal

t is time

As signal voltages are multiplied and then time-averaged, which has the effect of filtering out high frequencies, we can omit high frequency components from (3.2).

$$F = \cos\left(2\pi f\tau_g\right) = \cos\,(2\pi\frac{Dsin(\theta)}{\lambda}) \tag{3.3}$$

Where: λ is length of the incident wave

In the polar coordinates this fringe function for the ratio of $\frac{D}{\lambda} = 3$ is shown on the Figure 3.2.

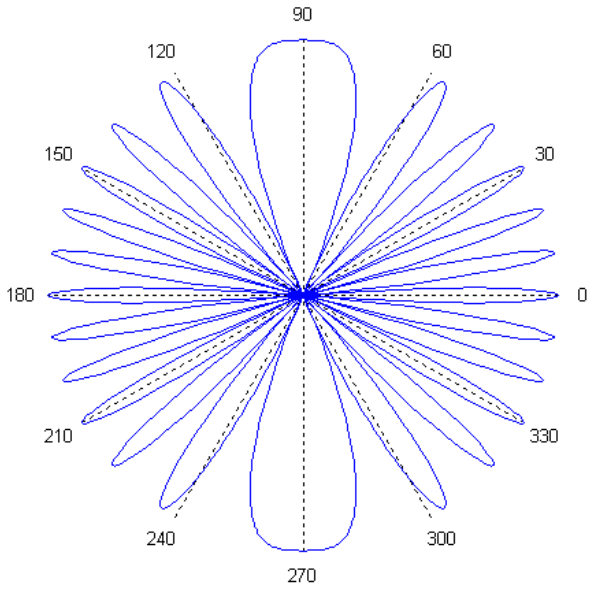

Figure 3.2 Fringe function $F = \cos(2\pi \frac{Dsin(\theta)}{\lambda})$ for the $\frac{D}{\lambda} = 3$ in the polar coordinates.

The fringe function is shown in the polar coordinates because such an approach actually represents the directional pattern of the power reception of the interferometer. However, to coincide with Figure 3.1, fringe function Figure 3.2 has to be turned on 90^0.

A holographic interferometer is used in many practical applications. For example measurements of displacements of objects with optically rough surfaces. These measurements can be applied to stress, strain and vibration analysis (Matsumoto et al., 2007; Taniguchi & Takagi, 1994). Especially interesting is the ability for non-destructive testing (Borza, 1998; Vincitorio et al., 2008). It can also be used to detect optical path length variations in transparent media, for example to visualize and analyse the temperature fields and velocity of currents in the gas chamber. (Andres et al., 1997; Kurosaki & Kashiwagi, 1990; Lee & Kim, 2004).

Radio interferometry has been used for decades to study the celestial sphere. The first radio interferometer with the dipole antenna arrays at 175 MHz and a baseline between 10 and 140 wavelengths was constructed in 1946 by Ryle and Vonberg to investigate a cosmic radio emission, which

had been discovered earlier(Ryle & Vonberg, 1946). The following decades brought a lot of interferometry applications.

3.3 Antenna setup requirements

To develop appropriate antenna element suitable for future applications of active 3-D microwave digital holography for breast cancer detection, one shall start from the system requirements. An ideal breast screening tool (Fear, Hagness et al., 2002) has to

- have a low health risk
- be sensitive to tumours and be specific to malignancies
- detect breast cancer at a curable stage
- be non-invasive and simple to perform diagnostics
- be cost effective and widely available
- involve minimal discomfort, so the procedure is acceptable to women
- provide easy to interpret, objective, and consistent results.

From here we may understand the requirements for the antenna setup. Keeping in mind all the above, we can resume that desirable setup to data acquisition has to provide the ability to effectively transfer information from the backscattered electromagnetic waves to the voltage on the inputs of the amplifiers and analogue to digital convertors. Now we can formalize the requirements for the Antenna Setup and finally for the Antenna element from the engineering point of view.

The level of health risk from the application using electromagnetic waves directly depends on the frequency of the illuminated waves and energy dissipated inside the patient's tissue. The most dangerous are applications that use an ionized frequency range as X-ray ("X-ray danger: get the big picture. Your cumulative radiation dose is growing. Do you really need to add to it?," 2006)[3]. Microwaves are non-ionizing radiation and danger from using microwaves depends mostly on the thermal effects due to

[3] Retrieved 12.04.2009, from http://www.ncbi.nlm.nih.gov/pubmed/17299871

electromagnetic energy dissipation and heating tissue (Johnson & Guy, 1972). Thus there is only one parameter we have to consider – how much energy we have to apply to get a clear backscattered signal.

Antenna setup should contain transmitting and receiving antennas. In the classical holography object under investigation (OUI) have to be illuminated by the plane wave as shown on the Figure 3.3.

Figure 3.3 Plane wave generated by transmitted antenna array TAA illuminates OUI.

This approach is hardly possible in our case because it requires a complex transmitting antenna array (TAA) consisting of multiple antenna elements with individual phase shift control for every transmitting antenna element. It has been reported that an indirect holographic technique can be used to reconstruct the complex aperture field of an antenna from a single scalar-intensity pattern (Smith et al., 2002). This approach allows generating of synthetic plane wave but involves a mechanical scanning system. The mechanical system, in turn, introduces its own problems and dramatically increases the data acquisition time. It is possible to use only one transmitting antenna as we are going to derive phase information using superheterodyne with phase lock loop circuitry from the same frequency source as the transmitting antenna. This circuitry will serve as the reference wave. Thus it was decided to use a spherical wave instead of planar and therefore one transmitting antenna (TA) as shown on the Figure 3.4.

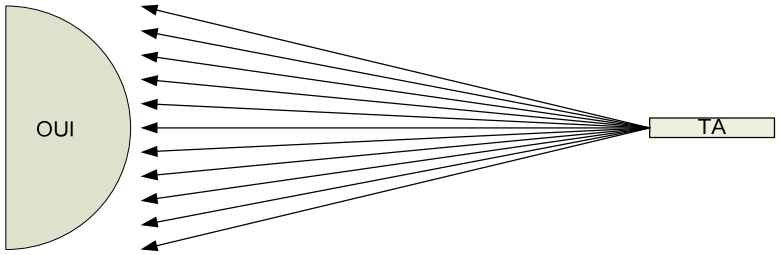

Figure 3.4 Spherical wave instead of planar generated by one transmitting antenna TA.

The receiving part of the antenna consists of multiple receiving antennas RA(i) placed on the determined positions. In Figure 3.5 reflections rays from only one point of space inside the OUI that introduce reflection interface are shown. We will discuss this later in detail.

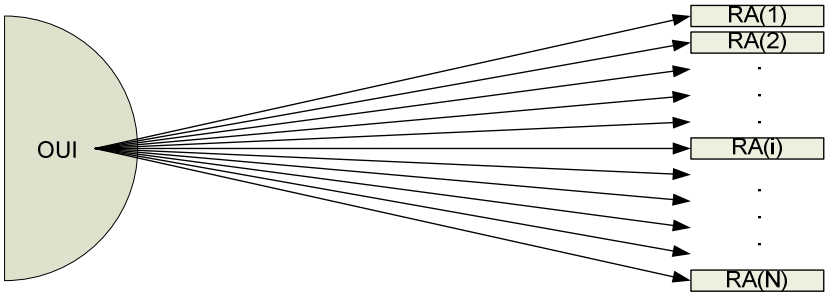

Figure 3.5 Receiving antennas RA(i) collecting reflected signal from the one of every points which introduce reflection interfaces.

3.4 Propagation media

Electromagnetic wave propagation speed depends on the refractive index of the propagation media.

$$v = \frac{c}{n} \tag{3.4}$$

Where: c is electromagnetic wave propagation speed in the vacuum

and n is refractive index

Refractive index for the lossless media

$$n = \sqrt{\varepsilon_r \mu_r} \tag{3.5}$$

Where: ε_r is material's relative permittivity.

and μ_r is material's relative permeability.

The wave propagation in the two different media shown in Figure 3.6 illustrates the dependency between the velocity of wave propagation and the wavelength.

Figure 3.6 Illustration of wave fronts in the context of Snell's law. Media below border horizontal line have ε_r higher then media above as result wave length visible as distance between concentric circles is shorter below border line and wave front and direction of beam shown by dashed line are changed (Courtesy Oleg Alexandrov).

One can see that changes in propagation speed leads to changes in the wavelength and wave front direction.

Snell's law states that the ratio of the sines of the angles of incidence and refraction is equivalent to the ratio of velocities in the two media, or equivalent to the inverse ratio of the indices of refraction.

$$\frac{\sin(\theta_i)}{\sin(\theta_t)} = \frac{v_i}{v_t} = \frac{n_t}{n_i} \tag{3.6}$$

Where: n_1 and n_2 are refractive index of the media

θ_1 and θ_2 are angles for beam in the media with refractive index n_1 and n_2 correspondently

and v_1 and v_2 are velocity of the beam in the media with refractive index n_1 and n_2 correspondently

These parameters are quite significant in our case not only because of the variations of the wavelength but also the direction of propagation is influenced. Another illustration of Snell's law given by equation (3.6) for nonmagnetic media can be seen on the Figure 3.7

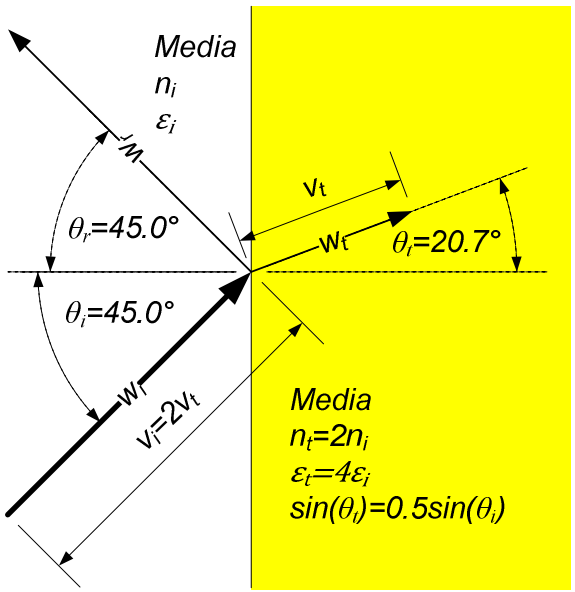

Figure 3.7 The illustration of Snell's law given by equation **(3.6)** for nonmagnetic media.

In Figure 3.7 the incident wave w_i from the media with refractive index n_i arrives to the boundary with media with refractive index n_t two times of the n_i after crossing the boundary velocity of the transmitted wave which became two times slower and the declination angle also became smaller in the manner that $\sin(\theta_t) = 0.5\sin(\theta_i)$. For nonmagnetic media it means that relative permittivity of the second media should be $\varepsilon_t = 4\varepsilon_i$.

Another fact doesn't shown on Figure 3.6 is that incident wave reflects partially from boundary between media that have different refractive index. It could be seen in Figure 3.7. The part of the incident wave is reflected from the boundary returns in the incident media with the same velocity so

with the same angle $\theta_r = -\theta_i$. The relationships between incident, transmitted and reflected waves are described by Fresnel equations. Fresnel determines reflection as

$$r = \frac{E_r}{E_i} \tag{3.7}$$

Where: E_i is amplitude of the incident wave

and E_r is amplitude of the reflected wave

And transmission

$$t = \frac{E_t}{E_i} \tag{3.8}$$

Where: E_t is amplitude of the transmitted wave

Here one has to take into account polarization of the incident wave and determine different representations for components of the incident wave parallel and perpendicular to the reflected boundary. The Fresnel equations for the component perpendicular to the boundary plane are for the reflection

$$r_\perp = \frac{n_i \cos(\theta_i) - n_t \cos(\theta_t)}{n_i \cos(\theta_i) + n_t \cos(\theta_t)} \tag{3.9}$$

Where: n_i is refractive index of the incident media

and n_t is refractive index of the transmission media

And for the transmission

$$t_\perp = \frac{2n_i \cos(\theta_i)}{n_i \cos(\theta_i) + n_t \cos(\theta_t)} \tag{3.10}$$

Reflection for the component parallel to the boundary

$$r_{\parallel} = \frac{n_i \cos(\theta_i) - n_t \cos(\theta_i)}{n_i \cos(\theta_i) + n_t \cos(\theta_t)} \tag{3.11}$$

And for the transmission component parallel to the boundary

$$t_{\parallel} = \frac{2n_i \cos(\theta_i)}{n_i \cos(\theta_t) + n_t \cos(\theta_i)} \tag{3.12}$$

Finally using Snell's law equation (3.6) we can express

$$\cos(\theta_t) = \sqrt{(1 - \left(\frac{n_i}{n_t}\sin(\theta_i)\right)^2} \tag{3.13}$$

Then equations (3.9) thru (3.12) will be seen as

$$r_{\perp} = \frac{n_i \cos(\theta_i) - n_t \sqrt{(1 - \left(\frac{n_i}{n_t}\sin(\theta_i)\right)^2}}{n_i \cos(\theta_i) + n_t \sqrt{(1 - \left(\frac{n_i}{n_t}\sin(\theta_i)\right)^2}} \tag{3.14}$$

$$t_{\perp} = \frac{2n_i \cos(\theta_i)}{n_i \cos(\theta_i) + n_t \sqrt{(1 - \left(\frac{n_i}{n_t}\sin(\theta_i)\right)^2}} \tag{3.15}$$

$$r_{\parallel} = \frac{n_i \cos(\theta_i) - n_t \cos(\theta_i)}{n_i \cos(\theta_i) + n_t \sqrt{(1 - \left(\frac{n_i}{n_t}\sin(\theta_i)\right)^2}} \tag{3.16}$$

$$t_{\parallel} = \frac{2n_i \cos(\theta_i)}{n_i \sqrt{(1 - \left(\frac{n_i}{n_t}\sin(\theta_i)\right)^2} + n_t \cos(\theta_i)} \tag{3.17}$$

Now taking into account equation (3.5) it becomes obvious that a bigger relative permittivity difference leads to the stronger reflected signal on the interface. Actually it is what we are going to measure to reconstruct the image but there are many other undesirable reflection interfaces on the way of the search signal. Multiple researches were done on the subject of dielectric properties of human tissue (Cole & Cole, 1941; Foster & Schwan, 1989; C. Gabriel et al., 1996). For the purposes of the current work a simplified model can be adopted. Let relative permittivity for air to

be $\varepsilon_{ra} = 1$, for skin $\varepsilon_{rs} = 36$, for under skin fibrous tissue $\varepsilon_{rf} = 9$. If the illumination wave arrives to OUI via air we will encounter the strongest reflection interface between air and skin. The same problem will occur on the way of backscattered signal. Only this interface can greatly attenuate useful energy arrived to the RA and produce a strong blurring signal. The only way to avoid this interface is to submerge the antennas and OUI into medium with $\varepsilon_r = 36$. There are few issues related this way. At first it is quite difficult to get an appropriate medium with $\varepsilon_r = 36$. Secondly the size of antennas becomes too small to produce repeatable antennas on the available production facilities, due to limited production technologies available for the current project. We have found trade off for this problem trying to resolve the problem of the second reflection interface. Second reflection interface appears between the skin and under skin fibrous tissue. And last but not least there would be an unavoidable interface between skin and inner tissue still remaining on the way of the signal. Thus we have taken into account the fact that skin thickness is much smaller than our wave length. If we use the transport medium with $\varepsilon_r = 9$, we will have double complementary interfaces and the thin skin layer should be transparent enough. Similar decisions with Electrical properties of used materials as shown in the table 3.1

Table 3.1. Initial dimensions for patch antenna

Media	ε_r	σ(S/m)
Breast tissue	9	0.4
Skin	36	4
Tumour	50	4
Immersion liquid	9	0

were reported (Fear, Meaney et al., 2003).

3.5 Frequency and Resolution

We are now going to apply astronomical imaging principles to medical purposes. Astronomical applications use a passive technique to reconstruct maps of celestial objects. We are going to use an active technique to reconstruct images of the human body for medical purposes. Thus we have to understand the differences, especially those ones which could cause obstacles on our way. To do so some explanations from astronomical literature (Thompson, 2007) will be considered with an additional abstraction level.

The angular resolution of the fringes may vary in dependency from the observation angle θ and is determined by the length of the baseline projected onto a plane normal to the direction of the arrived wave front (Thompson, 2007) and is interpreted as spatial frequency

$$u = \frac{Dcos(\theta)}{\lambda} \tag{3.18}$$

This value is opposite to the angular resolution. Angular resolution α in radians for the antenna array for the case when θ is very small and $cos(\theta)$is around 1 will be

$$\alpha = \frac{\lambda}{D} \tag{3.19}$$

Where: λ is the wavelength of the observed radiation

and D is the length of the maximum physical separation of the elements in the array. See Figure 3.1.

Linear resolution is one of the key parameters for the diagnostic imaging system. Two main limitations for resolution improvement are the size of

the antenna setup (AS), and the working frequency or more precisely the wave length of microwave.

As we are discussing the digital holography technique we can assume that the linear resolution of the developed system is determined by angular resolution of the antenna array (AA) and the distance between array and OUI. It is obvious from the geometric situation shown in Figure 3.8 that we can operate with these two parameters.

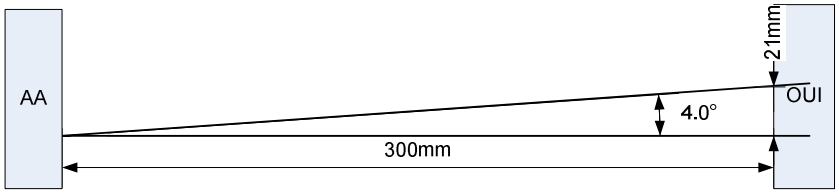

Figure 3.8 The linear resolution depends from angular resolution and distance between antenna array and OUI.

It is clearly seen from the equation (3.3) that a bigger distance between receiving antennas and shorter wavelength will give better angular resolution. However, there are some factors which can restrict selection of a very short wavelength. The main restriction factor is the electromagnetic properties of human breast. These properties were studied by the numerous researchers for decades (Duck, 1990; Swicord & Balzano, 2008). The most appropriate studies (S. Gabriel et al., 1996b; Lazebnik et al., 2007) limited the range for 1-20GHz. On the current stage we decided to stay within this range of frequencies mainly to avoid conductivity problems discussed in the section 2.3.

Thus being limited with a maximum frequency we have to select the maximum possible distance as a baseline between receiving antennas to get a better resolution again in accordance with equation (3.3). Selection of an appropriate maximum baseline is limited by external dimensions of the antenna setup and correspondent operating properties. As a starting point for calculation in the current work the maximum baseline size is set to 300mm to be inside reasonable external dimensions of the antenna setup.

Now to get resolution for example *21mm* with distance to OUI *300mm* and baseline *D = 300mm*, angular resolution around 4^o is needed as one can see from Figure 3.8.

Thus selection of reasonable baseline *D = 300mm* also determines maximum wave length of the exploration signal

$$\lambda \leq \frac{2\pi\alpha D}{360} \leq 20.8mm \qquad (3.20)$$

Taking into account that the length of electromagnetic wave is determined by

$$\lambda = \frac{\upsilon}{f} \qquad (3.21)$$

Where: υ is propagation speed of the electromagnetic wave

and f is frequency of the exploration signal

And from equations (3.4) and (3.5) one can derive required frequency as,

$$f = \frac{c}{\lambda\sqrt{\varepsilon_r \mu_r}} \qquad (3.22)$$

3.6 Proposed Antenna Setup construction

As previously discussed, air is not an optimal propagation media between AA and OUI due to big difference between dielectric constants of the air and human tissue. Most research groups working on the same problem come to the same decision. One of possible setup for data acquisition systems reported earlier (Fear, Li et al., 2002), shown in Figure 3.9. This setup requires the breast to be submerged into appropriate liquid with

$\varepsilon_r = 9$ while the patient is oriented in a prone position with the breast naturally extending through the hole in the examination table.

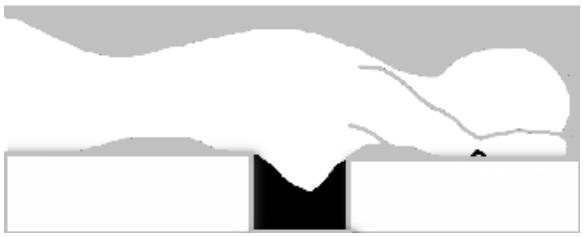

Figure 3.9 One of possible setup for data acquisition system. The breast naturally extending through a hole in the examination table and submerged into the liquid with $\varepsilon_r = 9$.

This requirement is not convenient for public medical institutions and not appropriate for patients with small breasts. We have decided to design a setup shown in Figure 3.10 using a solid medium with $\varepsilon_r = 9$. The patient is oriented in a supine position and the breast is flattened by AS.

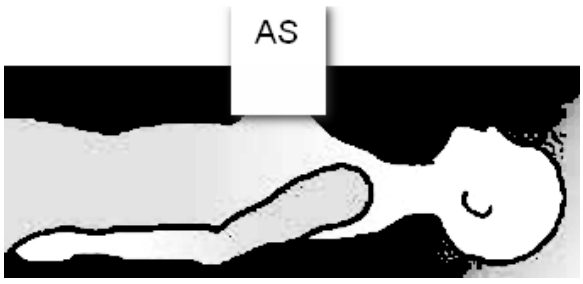

Figure 3.10 Setup for data acquisition system with solid medium. Breast is flattened by AS.

We believe that such approach will much better address requirements to

- be cost effective and widely available
- involve minimal discomfort, so the procedure is acceptable to women
- provide easy to interpret, objective, and consistent results.

In many cases it will be suitable to use such an antenna setup while the patient is in the vertical position. Besides this, the hygienic conditions for the suggested construction are better than for the construction with the liquid medium.

Let us compare the beam propagation models for the first and second setup shown in Figure 3.11 and Figure 3.12 correspondingly.

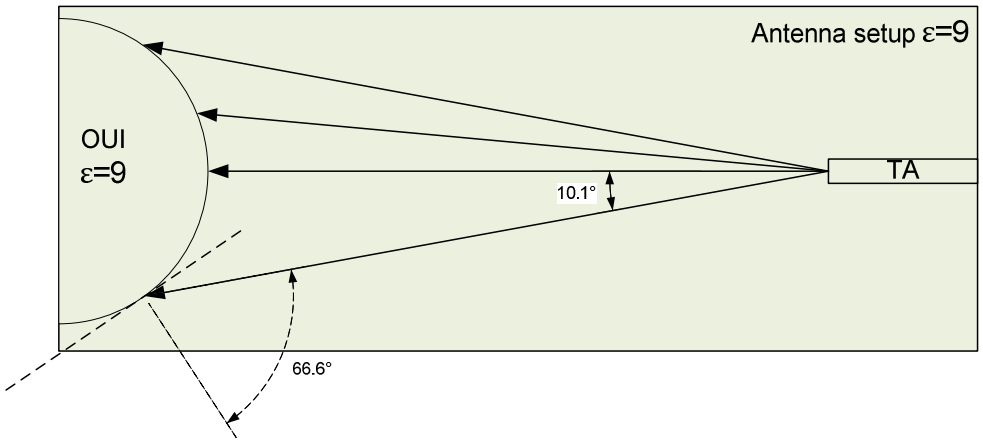

Figure 3.11 Practical example for the beam propagation model for the first setup.

Distance between TA and OUI is determined by the baseline. One can see a great difference in the angle between the incident beam and perpendicular to the skin for the very same beam arriving from the transmitting antenna to the OUI for cases presented in Figure 3.11 and Figure 3.12.

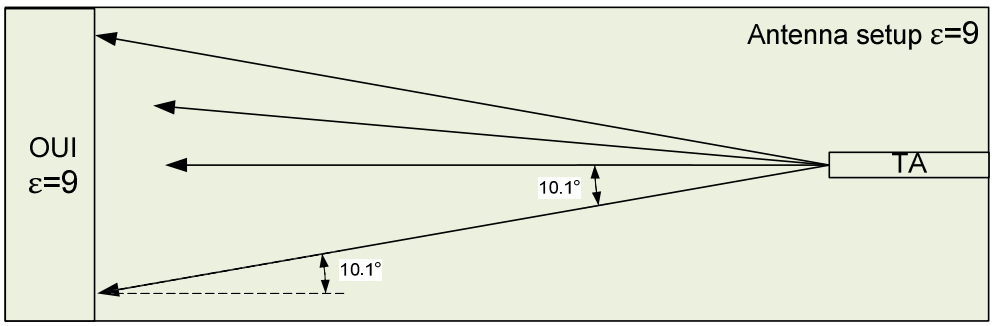

Figure 3.12 Practical example for the beam propagation model for the second setup.

This difference is significant for two reasons. Firstly there is always some difference in the refractive index between antenna setup and patient's tissue because different patients have a slightly different refractive index of the tissue due to its complicated nature. For a better understanding let's calculate the declination angle for two practical examples above to the

case when patient's tissue has a refractive index of 10% higher than antenna setup.

$$\alpha_1 = 66.6^o - \operatorname{asin}\left(\frac{\sin(66.6^o)}{1.1}\right) = 10.05^o \quad (3.23)$$

$$\alpha_2 = 10.1^o - \operatorname{asin}\left(\frac{\sin(10.1^o)}{1.1}\right) = 0.93^o \quad (3.24)$$

One can see that the suggested antenna setup gives a better result by an order of magnitude.

The second reason is related to the skin layer. Consider the geometrical situation shown in Figure 3.13.

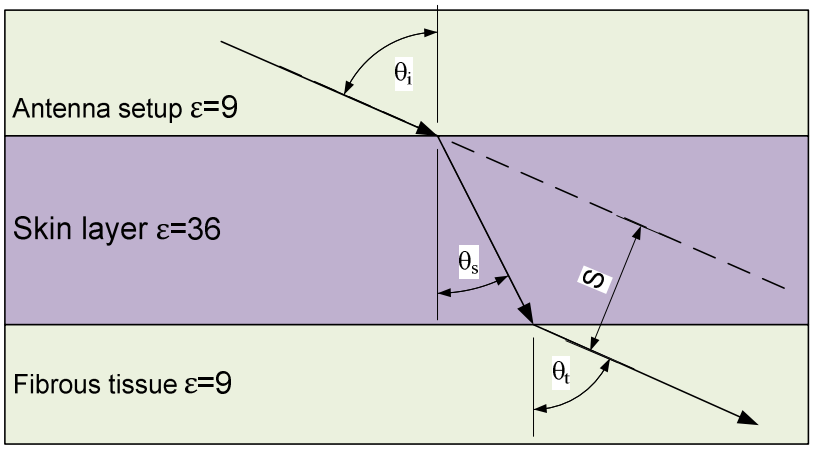

Figure 3.13 Shift of the beam in the skin layer.

Even if the refractive indexes of the patient's tissue and antenna setup totally coincide, the skin layer always exists and its relative permittivity greatly differs from the permittivity of the tissue. Even in an ideal case shown in Figure 3.13 we will have a shift in the beam path though the direction stays unchanged. Let's use practical examples from Figure 3.11 and Figure 3.12 to evaluate the amount of beam shift for a 2mm skin layer in accordance to the Figure 3.13

$$s_1 = \frac{2\sin\left(66.6^o - \operatorname{asin}\left(\frac{\sin(66.6^o)}{\sqrt{\frac{36}{9}}}\right)\right)}{\cos\left(\operatorname{asin}\left(\frac{\sin(66.6^o)}{\sqrt{\frac{36}{9}}}\right)\right)} = 1.43 \qquad (3.25)$$

$$s_1 = \frac{2\sin\left(10.1^o - \operatorname{asin}\left(\frac{\sin(10.1^o)}{\sqrt{\frac{36}{9}}}\right)\right)}{\cos\left(\operatorname{asin}\left(\frac{\sin(10.1^o)}{\sqrt{\frac{36}{9}}}\right)\right)} = 0.18 \qquad (3.26)$$

And once again the suggested antenna setup gives a better result by an order of magnitude.

Another problem consists of undesirable energy reflections from the external boundaries of antenna setup shown in Figure 3.7. To avoid this undesirable energy we can place microwave absorber materials around these boundaries. Using proper materials we can achieve working conditions for antenna setup similar to conditions in unbounded media.

The proposed antenna setup shown in Figure 3.10 corresponds to the requirements for the possible data acquisition system and can be used at the further development stage.

3.7 Distribution of antenna elements in array

Now we assume that we have backscattered microwave energy on the plane where the receiving antennas are situated. The next question is how to fix this energy for next reconstruction and analysis? We are going to use the Interferometry technique developed earlier for Radio Astronomy. Reconstruction of the image depends upon amount measurements of interference of waves which are collected by pairs of antennas. All possible distances between any two antennas in the array constitute the

bases set. The possible quality of the reconstructed image will depend directly on all possible distances between antenna elements in the array (Thompson, 2007). Number and placement of antenna elements are widely discussed in the literature (Cornwell, 1988; Hassan et al., 2005; Xi et al., 2008).

Let's consider some of the commonly used configurations of antenna arrays, and the boundaries of their autocorrelation functions. Autocorrelation functions are a widely used mathematical tool for finding repeating patterns, for example a periodic signal which has been blurred by noise especially in the case when the signal has a level much lower than the level of the noise. The simplest case of interferometer is shown in Figure 3.1. Sensitivity of such an array is limited by one spatial frequency determined by the base length. It is possible to get other spatial frequencies measured only by changing the base and making the next measurement. Kind of such an approach has been used in the indirect holographic technique (Elsdon et al., 2006). However this involves mechanical antenna positioning and dramatically increases data acquisition time for one patient.

To avoid this weakness one can use a linear array where antennas are located along a straight line. The simplest so called grating linear array has a uniform distribution of the antenna elements. Uniform distribution, especially in the linear array, is highly redundant because it represents a many of similar bases. Such redundancy in the using of the antenna elements leads to redundancy in the using of other expensive equipment such as amplifiers, detectors and analogue to digital convertors. However, those redundant measurements can be used as an aid in calibration of the instrumental response (Thompson, 2007). Another weakness of the linear array is foreshortened frequency coverage in the v dimension.

The last weakness can be addressed by two dimensional arrays. First and most obvious is a cross array which consists of two orthogonal linear arrays. In Figure 3.14 a configuration for cross array (left) and boundaries of the autocorrelation function for such an array (right) are shown. The

narrow extensions on the centres of the sides of the square represent parts of the autocorrelation functions of the individual arms, which are not formed in the cross-correlation of the arms (Thompson, 2007).

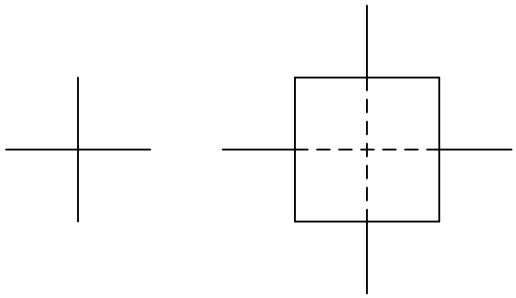

Figure 3.14 Configuration for cross array (left) and boundaries of the autocorrelation function for such an array (right). Figure adopted from (Thompson, 2007).

In Figure 3.15 a configuration for T shaped array (left) and boundaries of the autocorrelation function for such an array (right) are shown. Almost the same boundaries of the autocorrelation functions for the T array are determined by the identical spacing vectors because in the cross array Figure 3.14 for the first antenna pair, one antenna on the right arm and other antenna on the upper arm, there is a corresponding second antenna pair between the left and the bottom arms.

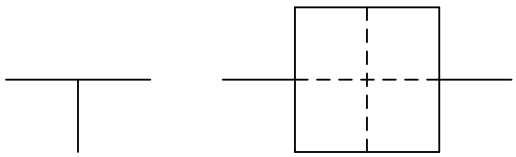

Figure 3.15 Configuration for T shaped array (left) and boundaries of the autocorrelation function for such an array (right). Figure adopted from (Thompson, 2007).

It is obvious that a T shaped array is less redundant then a cross array. However, with the same technical resources a Y shaped array with 120^o angle between arms shown on the Figure 3.16 left has even better boundaries of the autocorrelation functions because, as it is seen in Figure 3.16 right, shape of boundaries is closer to the circle.

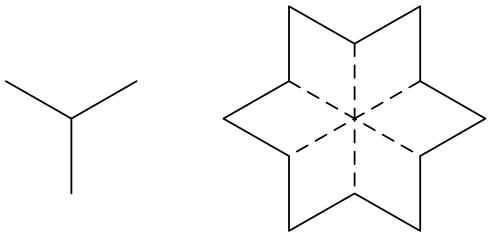

Figure 3.16 Configuration for Y shaped array (left) and boundaries of the autocorrelation function for such an array (right). Figure adopted from (Thompson, 2007).

A ring array shown in Figure 3.17 (left) provides such a distribution of antenna autocorrelation functions whose boundaries cuts off sharply in all directions at the circle diameter Figure 3.17 (right).

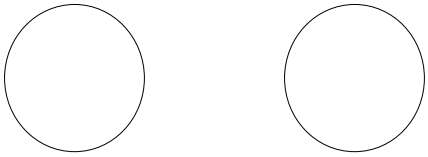

Figure 3.17 Configuration for ring array (left) and boundaries of the autocorrelation function for such an array (right). Figure adopted from (Thompson, 2007).

Ring array is so called a closed array configuration which is opposite to an open ended array configurations like considered before linear, cross, T and Y shaped arrays. Another well known representative of the closed configurations array consists of three equal circular arcs shown by the solid lines in Figure 3.18 left. This figure is called a Reuleaux triangle.

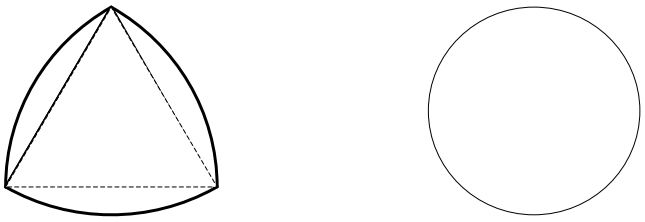

Figure 3.18 Configuration for Reuleaux triangle shaped array (left) and boundaries of the autocorrelation function for such an array (right). Figure adopted from (Thompson, 2007).

A Reuleaux triangle also has circular boundaries for the autocorrelation functions, Figure 3.18 right. It is so because a Reuleaux triangle has one

common property with a circle. The width of the Reuleaux triangle is constant in any directions. There are much more shapes with such property. Actually similar figures can be constructed for any regular polygon with an odd number of sides and all these shapes will have circularly boundaries for the autocorrelation functions.

There are number of parameters of interferometer arrays to be considered before proper selection. However, at this stage we will limit our selection by the requirements of the circular boundaries of the autocorrelation functions and uniformity of distribution in the spatial frequency coverage.

A ring array with regular distribution of antennas will produce regular distribution of the spatial frequencies. Figure 3.19 left merges regular antenna distribution in the xy plane and associated spatial frequencies distribution. Here triangles represent the antenna locations and the dots indicate the separations of all pairs of antennas. One can see that the circular array produces a sampling pattern that is too tightly packed in radius at large wave numbers and too tight in azimuth at small. In between the sampling is fairly uniform (Keto, 1997).

On the right side of Figure 3.19 uniform antenna distribution and correspondent separations of all pairs of antennas for the Reuleaux triangle is shown.

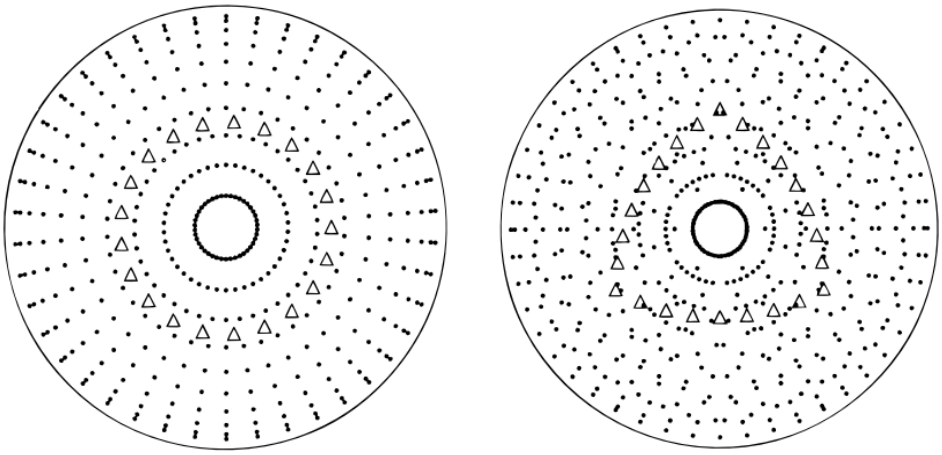

Figure 3.19 Sampling pattern for a circular array of 21 antennas left and for a symmetric array of 24 antennas in a Reuleaux triangle right. Figure adopted from (Keto, 1997).

One can see that differences in separations between antennas along the sides of the triangle and across the vertices create a less symmetric and much more uniform sampling pattern in Fourier space - Figure 3.19 right. It is obvious even at first glance that a Reuleaux triangle array has superior spatial frequency distribution. At a second glance we can see that some regularity and tightness still exists near the centre of the circle Figure 3.19 right.

This problem may be addressed by so called randomize shifting of the antennas around the initial placement as it is shown in Figure 3.20 right. Perturbations of the antenna locations away from a perfect Reuleaux triangle break down symmetry in the sampling pattern leading to more uniform coverage. Image of the spatial frequency distribution for the initial Reuleaux triangle array of 24 antennas is shown in Figure 3.20 left.

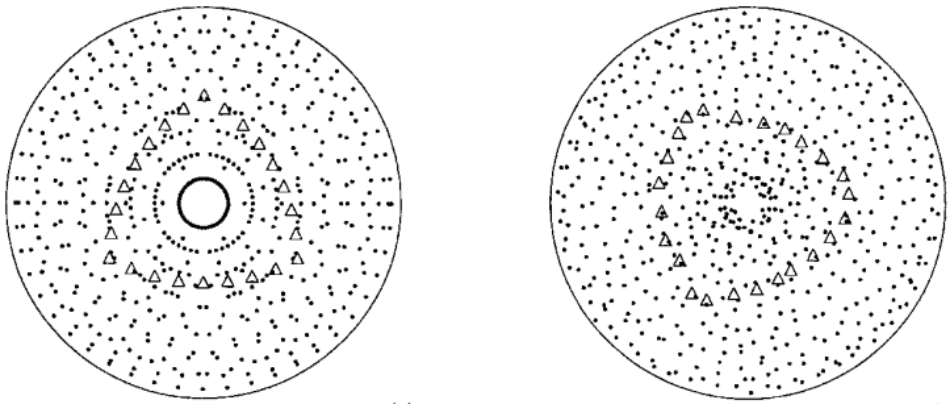

Figure 3.20 Sampling pattern for a symmetric array of 24 antennas in a Reuleaux triangle left and Triangular array of 24 antennas which has been optimized for the most uniform coverage by an elastic or neural net algorithm right. Perturbations of the antenna locations away from a perfect Reuleaux triangle break down symmetry in the sampling pattern leading to more uniform coverage. Figure adopted from (Keto, 1997).

Though the problem of the array optimization is beyond the scope of the current project, we have to think at least about boundary conditions. There are a number of optimization algorithms developed in recent decade (Cornwell, 1988; Hassan et al., 2005; Jin & Rahmat-Samii, 2008; Ruf, 1993) which can be used for the next stage. At this stage we can omit this decision because it will hardly put any additional condition on the antenna element. On the other hand the design of antenna element will definitely influence the smallest available base. Here we have to think not only about dimensions of the antenna element but also about the coupling problem which will be widely discussed in the next chapter.

3.8 Summary

The frequency and spatial dimensions of array will determine the maximum resolution achievable in the system. The resolution is also a factor of the distance from the array. Propagation media to be used in the antenna setup will also determine final dimensions as well as reflection and transmission conditions between antenna setup and patient body. Proposed antenna setup construction addresses many issues related to microwave imaging and could be used as a starting point for further development. Proper antenna element distributions have to be used to enhance image quality.

One more issue that has to be taken into consideration is that the side and back lobes of the transmitting and receiving antennas can interfere and significantly complicate the image reconstruction task. We are only interested in the measuring interference between backscattered waves.

Last but not least we have to keep in mind additional set of requirements. These include the patient's comfort and exploitation complexity as well as repeatability, robustness, required maintenance, price of production, which that all together will define accessibility and availability of target equipment.

Chapter 4 - Requirements for the Antenna element

Now when major requirements for the antenna setup are determined we may consider requirements for single antenna element such as the selection of polarization to be used and the required frequency range.

4.1 Introduction

A snapshot of the electromagnetic wave in the propagation media may be characterized by wavelength, amplitude and orientation. Adding the time dimension we may consider velocity of propagation and frequency. Projection of the wave on the plane orthogonal to the direction of propagation introduces the notion of polarization.

While maximum distance between antenna elements is determined by geometrical dimensions of array, minimal distance is determined by coupling between antenna elements. Thus the coupling issue has to be considered.

4.2 Frequency range of the antenna element

While the frequency of the electromagnetic wave is bounded with wavelength by equation (3.22) it is determined by the source. In our case it is determined by the source of electrical signal and in particular by its resonator. In developing an antenna element we should consider a frequency range rather than a single frequency because it is difficult to make two identical antennas.

On the other hand we have to consider the bandwidth, efficiency and quality factor. There is always a trade-off between them in arriving at an optimum antenna performance. The total quality factor is influenced by multiple parameters such as radiation, conduction, dielectric and surface wave losses (Balanis, 1997). In this section we consider only components related to the frequency range. There is a condition from the section 3.3 that antenna element has to be highly selective. Thus a quite narrow

bandwidth 3.3% was selected for current antenna that leads to higher total quality Q_t in that case for voltage standing wave ratio (VSWR) 2:1 in accordance to (Balanis, 1997)

$$\frac{\Delta f}{f_0} = \frac{1}{Q_t \sqrt{VSWR}} \tag{4.1}$$

Where: f_0 is middle frequency

and Δf is frequency range

Thus total quality will be

$$Q_t = \frac{1}{0.033\sqrt{2}} = 21.43 \tag{4.2}$$

Finally we have to select a middle frequency. As shown in section 3.5, resolution of the system directly depends on the signal wave length and thus from the frequency. The higher frequency gives better resolution with the same baseline. On the other hand, as shown in the section 2.3.2, the frequency is limited by the properties of the human tissue. The highest frequency 20 GHz has been determined in section 3.5. However there is other limitation related to “in house” manufacturing facilities.

To determine appropriate middle frequency on initial stage of this project several antenna elements for 10 GHz were manufactured and tested. Results of these measurements are beyond of scope of the current work. However they revealed a big difference for any two manufactured antennas. Such an approach would not allow providing appropriate validation of the analytical and modelling tools used in this project. It was clear that available manufacturing facilities do not allow reliable reproduction of the antennas for 10 GHz. To get more repetitive results the decision to use lower frequency was made and middle frequency 4.95 GHz was arbitrary selected.

To compare possible linear resolution on 10 GHZ and 4.95 GHz dependencies for these two frequencies were calculated and shown in the Figure 4.1.

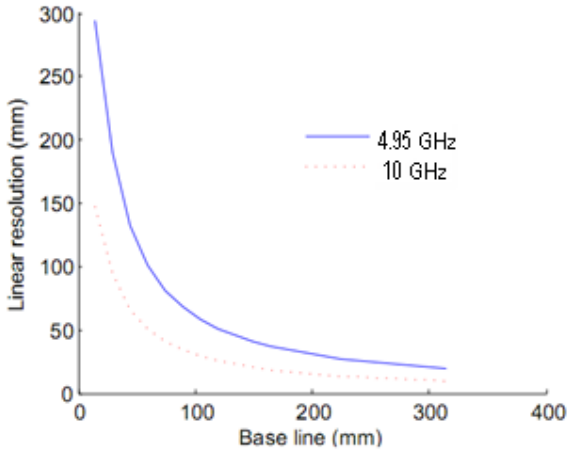

Figure 4.1 Dependencies of linear resolution for two frequencies 4.95 and 10 GHz from the distance between antenna elements.

It is obvious that dotted curve in the Figure 4.1 represents better linear resolution than solid curve.

4.3 Polarization

Polarization is other significant parameter of the electromagnetic wave. As it was mentioned above the electromagnetic wave may be characterized by wavelength, amplitude and orientation. In fact the polarization of antenna is the polarization of wave radiated by the antenna in a given direction (Stutzman & Thiele, 1997).

Linearly polarized waves and their projections on the plane normal to propagation direction, with vertical and horizontal polarization are shown in Figure 4.2 and Figure 4.3 correspondently as two ideal cases.

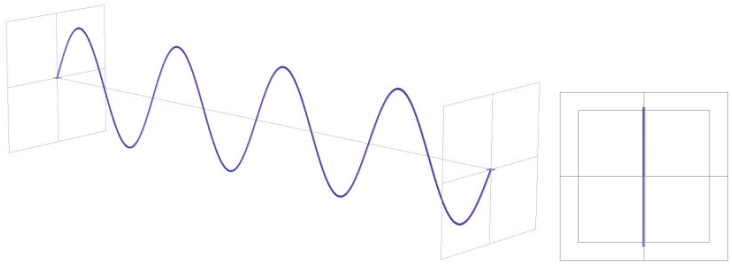

Figure 4.2 Linearly polarized wave with vertical polarization (left) and its projection on the plane normal to propagation direction.

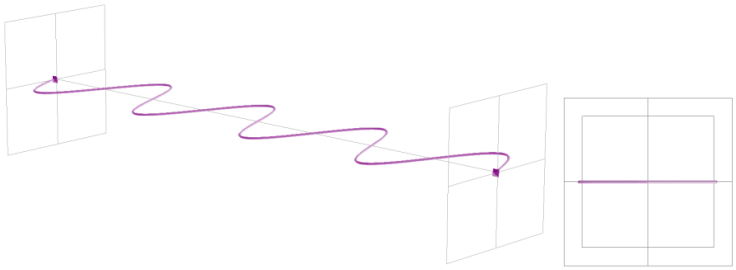

Figure 4.3 Linearly polarized wave with horizontal polarization (left) and its projection on the plane normal to propagation direction.

Superposition of these two linearly polarized waves will also be linearly polarized as shown in Figure 4.4.

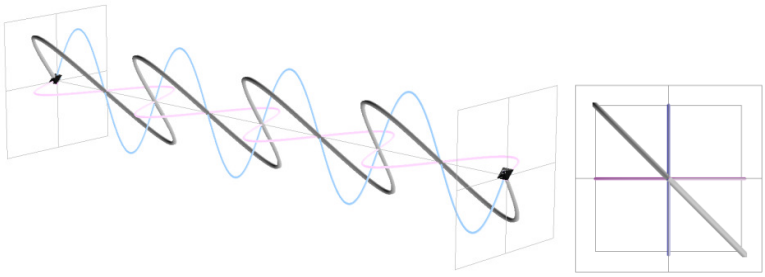

Figure 4.4 Superposition of these two linearly polarized waves (left) and its projection on the plane normal to propagation direction.

Linearly polarized waves have been called so after their projections on the plane which is normal to the propagation direction, because these projections are lines (Figure 4.4 right). Now if the phase difference between two originated waves is introduced, superposition of these two

linearly polarized waves becomes Elliptical and at the extreme Circular when phase difference is equal to $\pm 90^o$ as it is shown on the Figure 4.5.

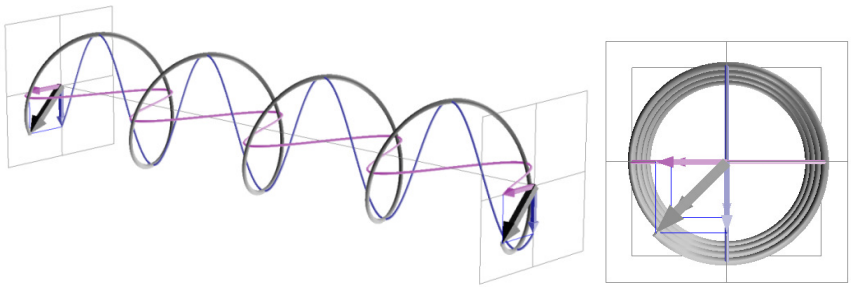

Figure 4.5 If phase difference between two originated waves is introduced superposition of these two linearly polarized waves becomes Elliptical and at the extreme Circular when phase difference is equal to $\pm 90^o$

The opposite statement is also true and any elliptically polarized wave may be decomposed in two linearly polarized waves. Phase difference $+90^o$ or -90^o will determine left or right hand polarisation. Selection of the left or right hand polarisation can be arbitrary for the current project.

As seen in Figure 4.2 and Figure 4.3, linearly polarized antenna can receive only the component of the electric field with the same orientation as the antenna. Therefore, due to the rotation of polarization of the reflected wave, using of the linear polarized antennas, the amount of energy collected on the receiving antennas will decrease. While it is possible to increase the power of the transmitted signal to compensate for losses from partially rotated polarization of the backscattered wave, this will lead to additional energy dissipating in the human tissue which is highly undesirable. To avoid this problem circularly polarized (CP) antenna type was proposed for the current antenna setup as more suitable to collect most of the electromagnetic energy crossing the antenna aperture by full use of the polarization components Figure 4.5 (Sergieiev & Kitaev, 2009).

4.4 Coupling

Mutual coupling is a quite complicated interaction between antenna elements in an array, especially when they are in close proximity.

Coupling is the result of desirable or undesirable energy transferring between neighbour antenna elements. As a result the current in a given antenna element depends on the current in all other nearby antennas as well as the voltage source at its own terminals. This leads to changes in the impedance at the terminals. The input impedance of single antenna isolated in unbounded media is

$$Z_{in} = \frac{V}{I} \tag{4.3}$$

Where: V is voltage on the antenna terminals

and I is current via the antenna terminals

The mutual input impedances of the antenna array depend upon many conditions as antenna type, polarization, and relative placement of antenna elements, type of feeds used to excite antenna elements, surface waves, media boundaries and so on.

We have to consider changes of array element impedance which depends on the array configuration and excitations. The relationship between the various currents and voltages are given by the network relationships (Stutzman & Thiele, 1997)

$$\begin{cases} V_1 = Z_{11}I_1 + Z_{12}I_2 + \cdots + Z_{1N}I_N \\ V_2 = Z_{21}I_1 + Z_{22}I_2 + \cdots + Z_{2N}I_N \\ \vdots \\ V_1 = Z_{N1}I_1 + Z_{N2}I_2 + \cdots + Z_{NN}I_N \end{cases} \tag{4.4}$$

Where: V_n is voltage on the $n\text{-}th$ antenna terminals

I_n is current via the $n\text{-}th$ antenna terminals

Z_{nn} is the self impedance of the $n\text{-}th$ antenna element when all other elements are open circuited

and Z_{mn} is the mutual impedance between the $n\text{-}th$ the $m\text{-}th$ antenna elements when all other elements are open circuited

The mutual impedance Z_{mn} between the $n\text{-}th$ the $m\text{-}th$ antenna elements is the open circuit voltage produced at the first terminal pair divided by the current supplied to the second when all other terminals are open circuited

$$Z_{mn} = \frac{V_m}{I_n} \,|I_i = 0 \text{ for all } i \text{ except } i = n \tag{4.5}$$

To simplify the analysis let's assume that the antenna system consists of two linear antenna elements and correspondently four terminals as shown in Figure 4.6.

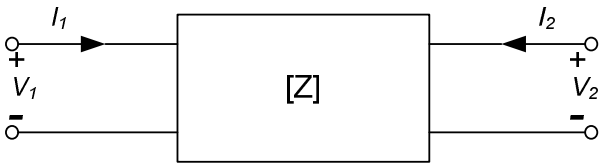

Figure 4.6 System of two antenna elements. Figure adopted from (Stutzman & Thiele, 1997).

Equation system (4.4) will shrink to

$$\begin{cases} V_1 = Z_{11}I_1 + Z_{12}I_2 \\ V_2 = Z_{21}I_1 + Z_{22}I_2 \end{cases} \tag{4.6}$$

Then the input impedance at port #1 with port #2 open-circuited is:

$$Z_{11} = \frac{V_1}{I_1} \,|I_2 = 0 \tag{4.7}$$

The mutual impedance at port #1 due to a current at port #2 with port #1 open-circuited is:

$$Z_{12} = \frac{V_1}{I_2} \,|I_1 = 0 \tag{4.8}$$

The mutual impedance at port #2 due to a current in port #1 I with port #2 open-circuited is

$$Z_{21} = \frac{V_2}{I_1} \,|I_2 = 0 \tag{4.9}$$

And the input impedance at port #2 with port #1 open-circuited is

$$Z_{22} = \frac{V_2}{I_2} \,|I_1 = 0 \tag{4.10}$$

Figure 4.6 also can be seen as its T-equivalent shown in Figure 4.7.

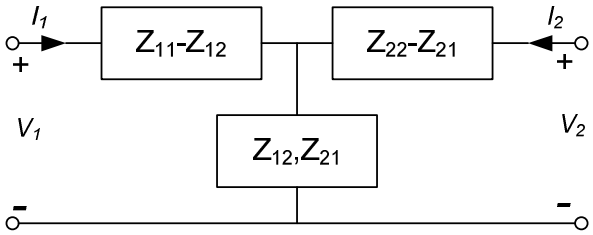

Figure 4.7 T-equivalent of the two antenna array. Figure adopted from (Stutzman & Thiele, 1997).

Now total voltage at the first antenna terminals can be written

$$V_1 = Z_{11}I_1 + Z_{12}I_2 \tag{4.11}$$

Voltage at the second antenna terminals can be written

$$V_2 = Z_{21}I_1 + Z_{22}I_2 \tag{4.12}$$

If we attach load impedance to the second antenna terminals as shown in Figure 4.8

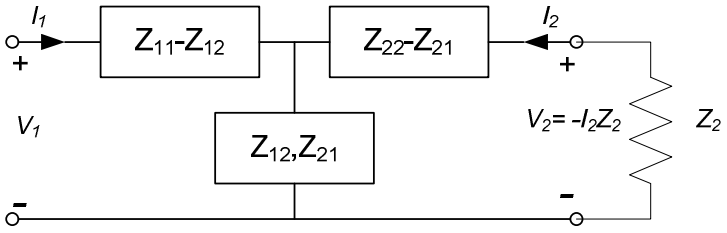

Figure 4.8 T-equivalent of the two antenna array with loaded second antenna. Figure adopted from (Stutzman & Thiele, 1997).

We can express input impedance of the first antenna via the load at the unexcited terminals of the second antenna Z_2 and the two self impedances Z_{11}, Z_{22}, and the mutual impedance Z_{12}. Substituting V_2 in the equation (4.12) and solving for the I_2 we can derive

$$I_2 = -\frac{Z_{21}I_1}{Z_{22}+Z_2} = -\frac{Z_{12}I_1}{Z_{22}+Z_2} \tag{4.13}$$

Now we can determine input impedance for the first antenna as

$$Z_{1.in} = \frac{\mathrm{V_1}}{\mathrm{I_1}} = \mathrm{Z_{11}} - \frac{(\mathrm{Z_{12}})^2}{\mathrm{Z_{22}}+\mathrm{Z_2}} \tag{4.14}$$

Often it is necessary to measure antenna parameters in the array. Assuming we have two half wavelength dipole antennas on resonant frequency and looking on the equation (4.14) we can do such a measurement for $\mathrm{Z_{11}}$while leaving second antenna terminals free, i.e. if $\mathrm{Z_2} = \infty$. In the same manner we may measure $\mathrm{Z_{22}}$ and then using short circuit between second antenna terminals and measuring $Z_{1.in}$ determine Z_{12} as

$$Z_{12} = \sqrt{Z_{22}(Z_{11} - Z_{1.in})} \tag{4.15}$$

For the purposes of the current project, deviation in the impedances is very significant because, as it will be shown later, phase shift in the received signal depends on relation between real and imaginary parts. On the other hand, the phase is value which will give information for the subsequent image reconstruction.

As mentioned in the beginning of current section mutual currents and correspondently impedances are dependent on many conditions. Let us compare impedances for two dipole antenna array shown in Figure 4.9.

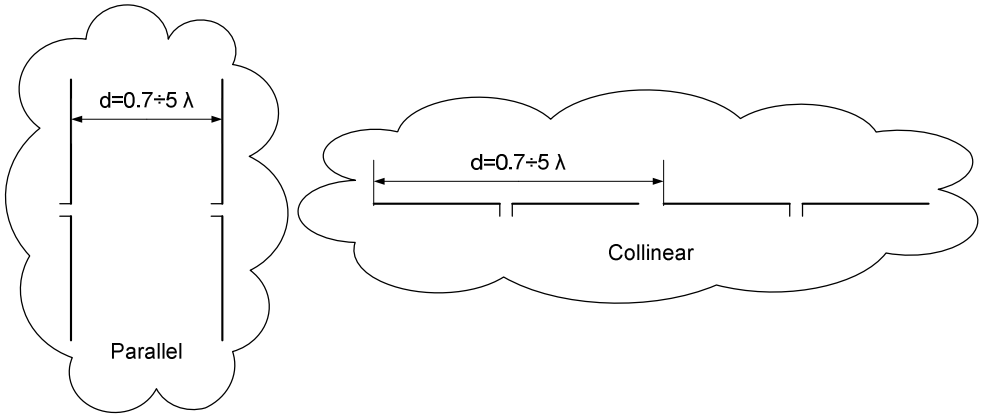

Figure 4.9 Two dipole antenna arrays. Parallel (on the left) and Collinear (on the right).

The dependencies of input impedance from the separation distance for Parallel and Collinear orientation arrays on the target frequency in the unbounded media were obtained by the means of modelling tool described in Chapter 5.

For better comprehension let us separate real and imaginary part and represent in different figures. In Figure 4.10 the dependencies for the real part of input impedance are shown. Dotted lines represent reference impedance for the single antenna on the same frequency.

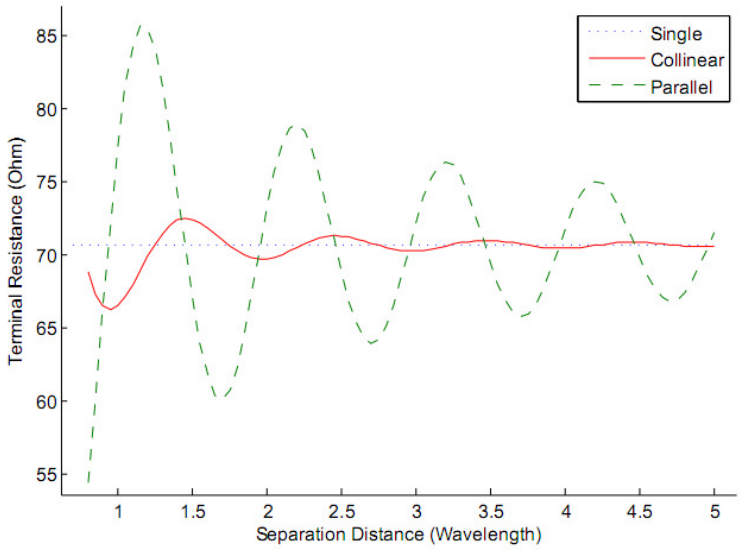

Figure 4.10 The real parts of the dependencies from the separation distance for Parallel and Collinear orientation arrays on the resonance frequency in the unbounded media as shown in Figure 4.9. Dotted line represents resistance for the single antenna on the same frequency.

The dependencies for the imaginary part are shown in Figure 4.11.

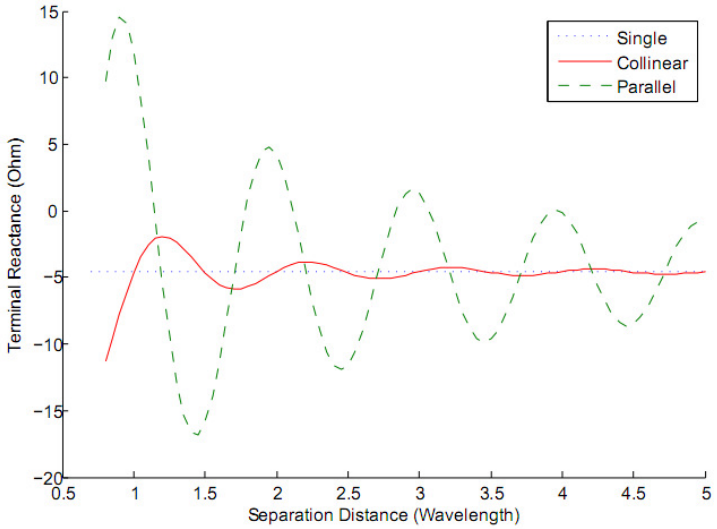

Figure 4.11 The imaginary parts of the dependencies from the separation distance for Parallel and Collinear orientation arrays on the resonance frequency in the unbounded media as shown in Figure 4.9. Dotted line represents reactance for the single antenna on the same frequency.

It is seen from Figure 4.10 and Figure 4.11 that mutual impedances for both real and imaginary parts vary around reference values for single antenna and the absolute value of deviation declines with increasing of the

separation distance between antennas. It is also clearly seen that the absolute value of the mutual coupling is much higher for parallel antenna placement in comparison to the collinear placement. The reason for the last difference is in the directivity radiation pattern of the dipole. It is obvious from Figure 4.12, where distances between antennas for parallel and collinear orientation are similar, that radiation fields are overlapping much more for parallel dipoles then for collinear.

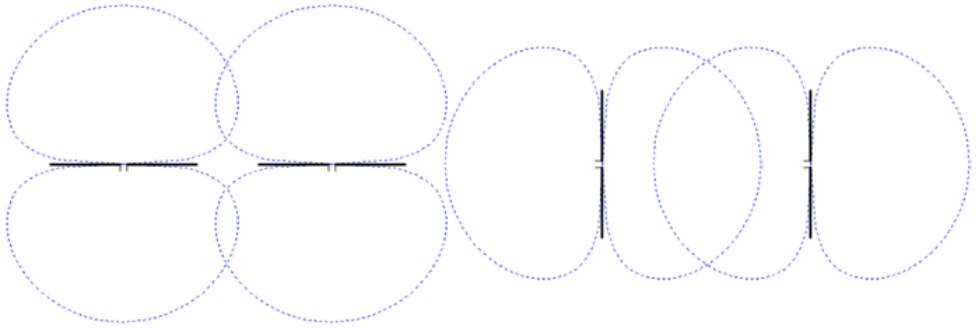

Figure 4.12 Radiation patterns of two dipole pairs.

For comparison the directivity radiation pattern for patch antennas is shown in Figure 4.13.

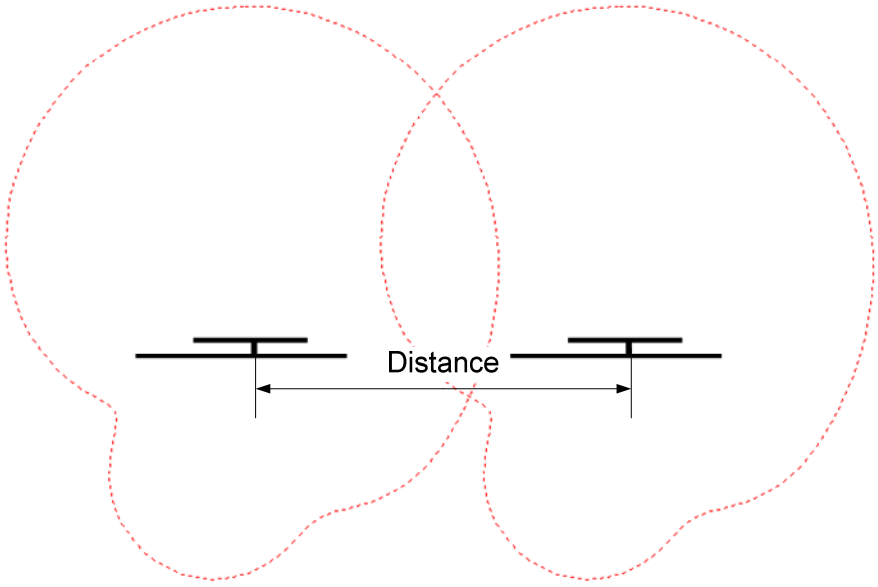

Figure 4.13 Calculated radiation pattern for patch antennas.

These directivity radiation patterns were obtained by the means of modelling tool described in Chapter 5.

In the chapter 6 we will explore mutual impedances for patch antennas in more details.

4.5 Summary

In this chapter, the main requirements such as frequency range and polarization type for the antenna element, as well as mutual coupling issue related to the antenna array have been considered. A desirable antenna element has to have circular polarization. The next condition is that the antennas have to be highly selective. This condition is well agreed with the holography technique, and possible limitations would depend on the quality of modelling and production facilities.

Chapter 5 - Antenna Design

5.1 Design Flow and Methodology

There is always a trade-off between technical rigor and time to research and funds available. It is difficult to satisfy the requirements for contemporary antenna design using only either theoretical analysis or empirical cut and try approaches. The most useful tools for today's antenna design are electromagnetic modelling tools. There are many of electromagnetic modelling software tools available to help with designing complex antennas. A careful balance of analytical, modelling and empirical approaches can provide an acceptable solution. The following describes a methodology that has been used to design antenna element for microwave imaging for medical purposes. There are six parts to the method:

- Requirements analysis of the Antenna
- Selection and validation of appropriate modelling tool
- Selection of basic antenna design
- Modelling,
- Samples production
- Measurement for comparison to desirable metrics.

Requirements for the antenna element were given in the Chapter 4. Thus we can move to the selection of the modelling tool.

5.2 Selection and validation of appropriate modelling tool

There are many comprehensive tools for microwave simulation on the market today. For example, Ansoft High Frequency Structure Simulator[4] is the industry-standard simulation tool for 3-D full-wave electromagnetic field simulation. This standalone product even has such intrinsic engineering design tools as an automated solution process. However, the

[4] *ANSOFT HFSS.* (2009). Retrieved 30.07.2009, from http://www.ansoft.com/products/hf/hfss/

price of this product makes it unavailable for the current project. Other powerful tools include the COMSOL Multiphysics®[5] which is able to complete multiphysics simulation but is still too expensive for one project. Due to limited financial ability the current job has to be done with the aid of freely available electromagnetic modelling software. Among other available software the MATLAB Antenna Toolbox (MAT) (Makarov & Kempel, 2005) was selected because of sufficient functionality, well organized documentation, and a traceable history back to 2002 when the previous version was accompanied by the book (Makarov, 2002).

MAT is a tool for the modelling of basic metal-dielectric antennas and resonators based on the Method of Moments. The Method of Moments used in this software relies on Rao-Wilton-Glisson (RWG) edge elements (Rao et al., 1982). Initially the surface of a metal antenna under study is divided into separate triangles (mesh) as shown in Figure 5.1 to establish a matrix of vector basis functions associated with every interior edge (i.e., no boundary edge).

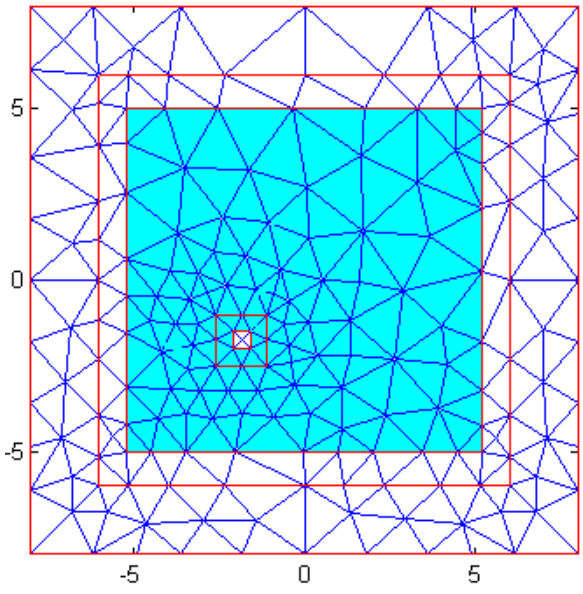

Figure 5.1 Example of 2-D mesh generated by PDE tool box.

[5] *COMSOL Multiphysics®*. (2009). Retrieved 30.07.2009, from http://www.comsol.com/products/multiphysics/

Consider a simplified geometrical situation shown in Figure 5.2 (Rao et al., 1982) with each pair of triangles from the metal surface having a common edge constituting the corresponding RWG edge element

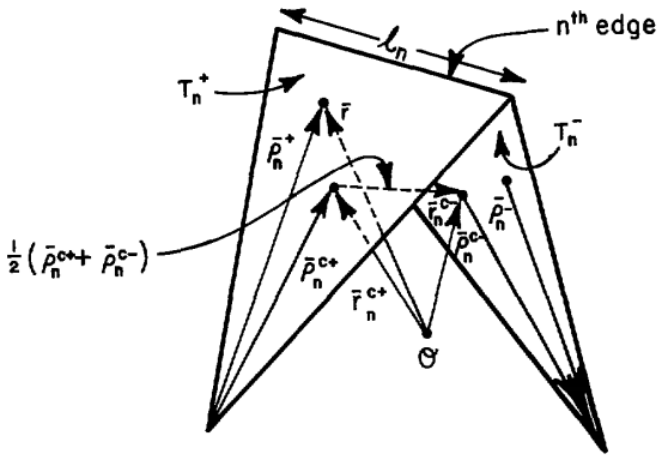

Figure 5.2 Schematic of a RWG edge element. Triangle pair and geometrical parameters. Figure is adopted from the (Rao et al., 1982).

One of the triangles has a plus sign T_n^+ and the other a minus sign T_n^-. Points in T_n^+ may be designated by the position vector ρ_n^+ defined with respect to the free vertex of T_n^+ Similar remarks apply to the position vector ρ_n^- except that it is directed toward the free vertex of T_n^-. The plus or minus designation of the triangles is determined by the choice of a positive current reference direction for the *n*-th edge, the reference for which is assumed to be from T_n^+ to T_n^-. The vector basis function associated with the *n*-th edge

$$fn(r) = \begin{cases} \frac{l_n}{2A_n^+}\rho_n^+, & r\ in\ T_n^+ \\ \frac{l_n}{2A_n^-}\rho_n^-, & r\ in\ T_n^- \\ 0, & otherwise \end{cases} \tag{5.1}$$

where l_n is the length of the edge,

and $A_n^{\pm}$ is the area of triangle $T_n^{\pm}$

The basis function (5.1) of the edge element approximately represents the surface current, which corresponds to a small but finite electric dipole. Thus the division of the antenna structure into RWG edge elements approximately corresponds to the division of the antenna into small electric dipoles. A more detailed explanation of how Method of Moments was implemented in the modelling software is given in (Makarov, 2002). For the current work it is significant that we can model basic parameters for developed antenna element and visualize them with Matlab representation tools.

Validation of the modelling tool especially for the non commercial tools is the most difficult part in the overall tool selection process. In our case we can complete validation by manufacturing of the antenna elements and measuring their parameters.

5.3 Selection of basic antenna design

We have selected circular polarization for our application thus we have to consider only appropriate antenna types. There are quite a few candidates for the basic type of our antenna element.

As mentioned in section 4.3 circular polarization is determined by the equity of two orthogonal linear components with a phase shift of 90^o. There are several ways to achieve such composition. First and most obvious it is to use two orthogonal linearly polarized antennas like dipole, Bowtie or Vivaldi antennas with phase shift of 90^o between feeding currents. The second way is using helical, spiral or conical antennas which may emit almost a pure circularly polarized wave in certain conditions by using one feeding point. The third way is using patch antennas. Here we should consider both variants, with two and singular feeding points.

Cross dipole antenna and its radiating pattern are shown in Figure 5.3

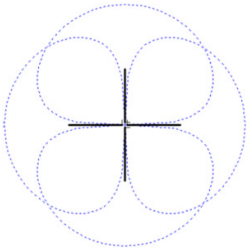

Figure 5.3 Cross dipole antenna and its radiating pattern.

If these two dipoles are feeding with equal amplitude and phase shift between feeding currents 90^o then a circularly polarized wave will propagate in the direction perpendicular to the figure plane. Similar types of antennas are used with frequencies below 1 GHz for example in airport to airplane communication (Brown & Woodward, 1947).

In the microwave range suitable for medical purposes, among circularly polarized cross type antennas we can found cross Bowtie (Yun et al., 2005) and cross Vivaldi (Zhang et al., 2009) antennas shown in Figure 5.4 and Figure 5.5 correspondingly.

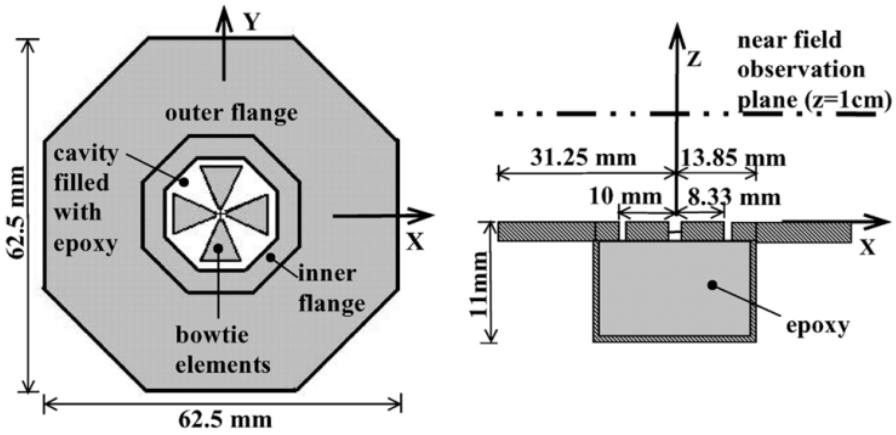

Figure 5.4 Cross Bowtie antenna. Figure adopted from (Yun et al., 2005)

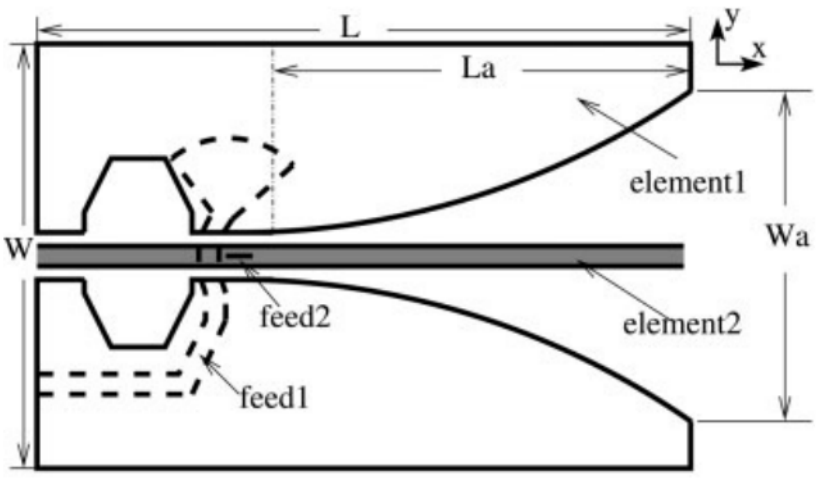

Figure 5.5 Cross Vivaldi antenna. Figure adopted from (Zhang et al., 2009)

These antennas are gave fairly good results. Their strength is in the wide frequency range. However, one can imagine difficulties related to producing multiple identical samples of these antennas required for our antenna setup. Moreover most difficult manufacturing problem is the construction of a feeding point of such antennas. The size is quite small compared to the required accuracy. An attempt to achieve phase shift between feeding currents 90^o leads to complex feeding circuitry. Detailed consideration of such feeding circuitry is beyond of the scope of the current work but our own attempt to reproduce antenna from (Yun et al., 2005) shown in Figure 5.6 was unsuccessful and gave us a good understanding of the difficulties relating to the construction itself and to the feeding point reproduction in particular.

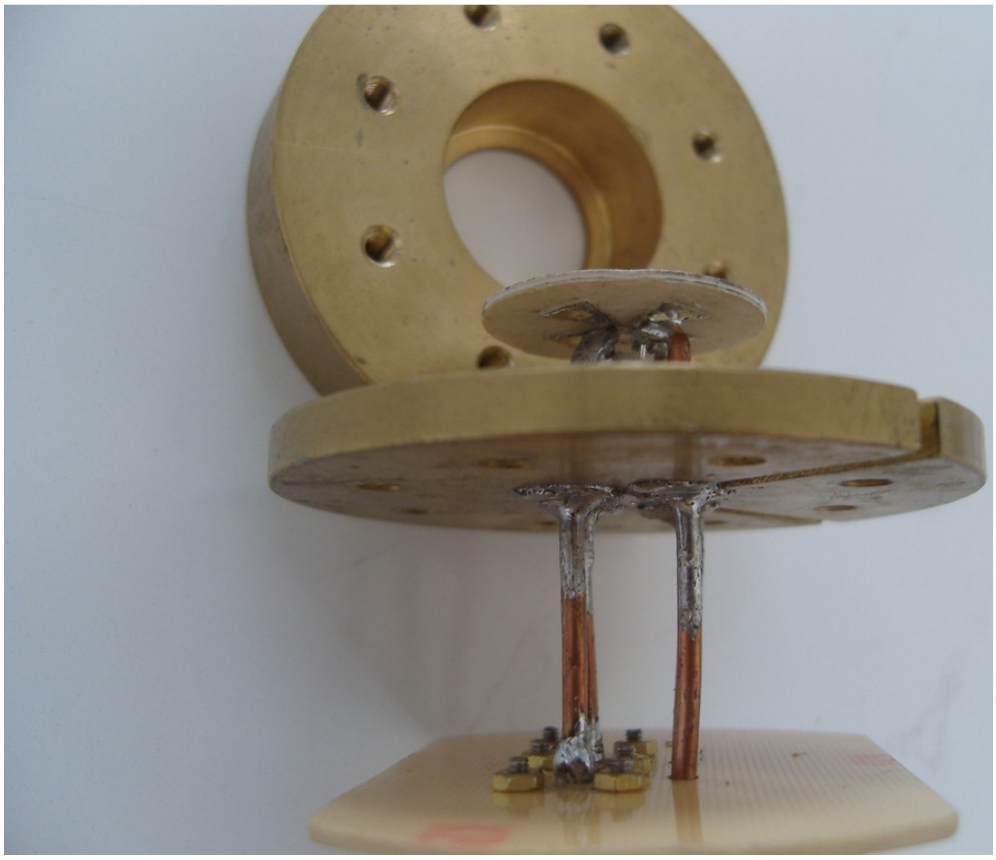

Figure 5.6 Cross Bowtie antenna manufactured by drafts from (Yun et al., 2005)

Micro strip technology gives a wide range of possible configurations for circularly polarized radiator constructions. Antenna designers use different perturbations such as truncated corner, diagonal or cross slots in the patch centre to excite two modes in a one feed design. It is also supposed to be efficient to employ an asymmetric location of the feed and to use nearly square patches, i.e., patches with a small difference of the side lengths (Semouchkina et al., 2004). Let's consider some of them for better choice selection.

Array to Generate Circular Polarization with Linearly Polarized Elements (Huang, 1986) is shown in Figure 5.7.

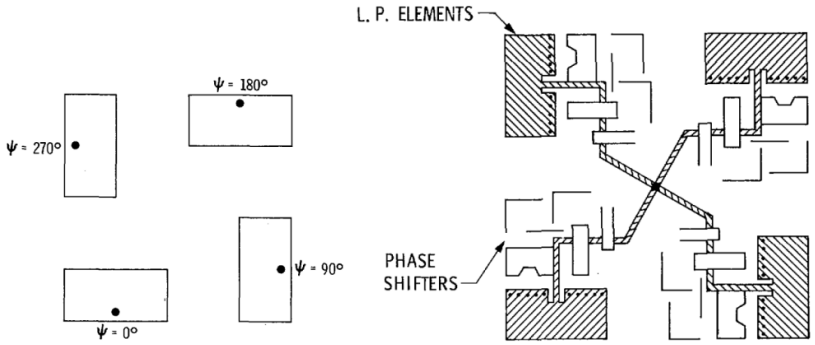

Figure 5.7 Array to Generate Circular Polarization with Linearly Polarized Elements. Figure is adopted from (Huang, 1986).

This approach appears would require a large area in the array of antennas. This would lead to a limited number of elements in the array. That in turn may become problematic from point of view providing optimal data acquisition.

There are a number of the circularly polarized slot antennas reported (R. P. Xu et al., 2007; Zhao et al., 2008) for example. One of the reported slot antennas is represented in Figure 5.8.

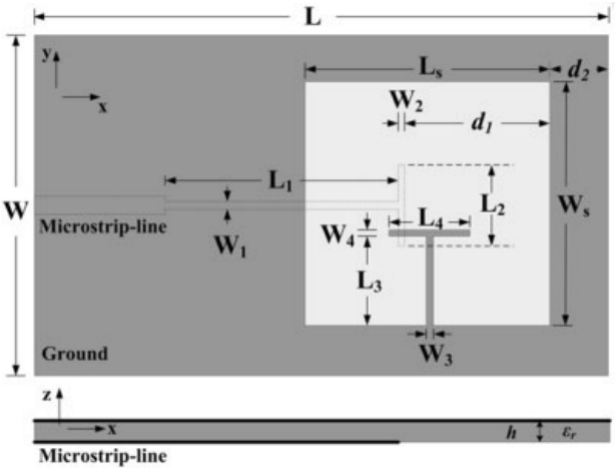

Figure 5.8 Circularly polarized wide slot antenna. Figure is adopted from (R. P. Xu et al., 2007)

This type has less area at first glance. One of undesirable properties in our case for this antenna is back lobe in the direction pattern.

For the square patch, required circular polarization can be obtained if two orthogonal modes are excited with a 90^0 time-phase difference between

them (Balanis, 1997). It requires two feeding points and a quadrature coupler. This leads to a complicated optimization procedure and additional area consumption. Thus this type of antenna has been excluded from consideration in the current project.

Cross polarized antennas appear to be difficult in production especially feeding circuitry for circular polarization. Spiral or Conical antenna omitted due limitations of available modelling tools and production facilities. Due to limited antenna array dimensions and previously selected modelling tool constraints, on the final stage of the appropriate antenna element selection only two patch antenna types were considered. Namely the square patch with truncated corners and near square patch antenna. Moreover both named antenna types make it possible to equate the length of path from the antenna elements to the signal amplifier and digitizer what is highly desirable for the purposed measurement technique. It is suitable to use probe feeding circuitry with such antenna types. Near square patch antenna has better analytical subscription and allow a simpler mathematical model in comparison with a square patch with truncated corners. Thus the near square patch antenna type has been selected as the basic antenna element design.

A detailed discussion of other antenna types is outside of the scope of this project. Further we will describe in more detail the modelling and optimization of circularly polarized near square patch antenna.

5.4 Modelling of the Antenna element

5.4.1 Theoretical background

For patch antenna, CP can be accomplished by adjusting the physical dimensions of the patch and using either single or two or more feeds (Balanis, 1997). The most direct way is to use two separate orthogonal feeds to excite a square-patch antenna. The current work used a single feed to generate two orthogonal modes on the nearly square patch. To meet the necessary conditions for circular polarization, the dimensions of

the patch and position of the feeding point must ensure that the magnitudes of the two modes are equal. We have started our modelling with selected a basic antenna design represented in Figure 5.9.

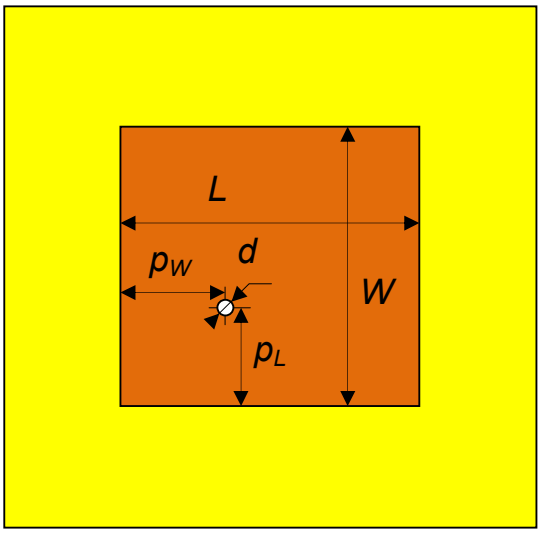

Figure 5.9 Near square patch antenna sketch and variable dimensions for selected basic antenna design, up-down view.

Interdependency between length and width for this antenna type is given by (Balanis, 1997)

$$L = W(1 + \frac{1}{Q_t}) \tag{5.2}$$

where L is length

W is width of the patch

and Q_t is quality factor

Quality factor has been determined in the section 4.2, thus the required ratio between patch sides is

$$\frac{L}{W} = 1 + \frac{1}{Q_t} = 1.047 \tag{5.3}$$

To select actual initial dimensions for our antenna model let's consider Figure 5.10. Due to finite dimensions of the patch the fields at the edges of

the patch undergo fringing. Fringing effects make the patch electrically be greater than its physical dimensions.

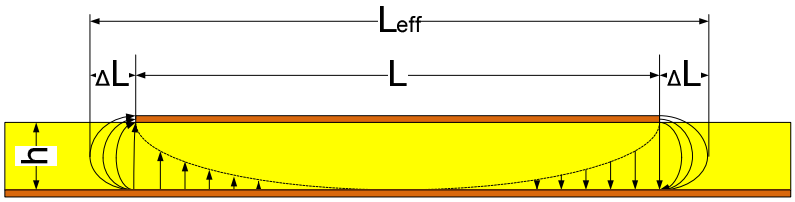

Figure 5.10 Patch antenna side view. Effective patch dimensions are greater than its physical dimensions because of fringing effects.

Figure 5.10 shows that effective dimensions of the patch are

$$L_{eff} = L + 2\Delta L \tag{5.4}$$

$$W_{eff} = W + 2\Delta W \tag{5.5}$$

Thus the physical dimensions of patch could be derived from required frequencies dielectric and magnetic properties of materials (Balanis, 1997).

$$L = \frac{1}{1f_L\sqrt{\varepsilon_{reff}}\sqrt{\mu_0\varepsilon_0}} - 2\Delta L \tag{5.6}$$

$$W = \frac{1}{1f_W\sqrt{\varepsilon_{reff}}\sqrt{\mu_0\varepsilon_0}} - 2\Delta W \tag{5.7}$$

ΔL and ΔW could be derived from empirical equations(Kirschning et al., 1981)

$$\frac{\Delta L}{h} = \frac{\xi_1\xi_3\xi_5}{\xi_4} \tag{5.8}$$

With

$$\xi_1 = 0.434907 \frac{\varepsilon_{eff}^{0.81} + 0.26}{\varepsilon_{eff}^{0.81} + 0.189} \frac{\left(\frac{W}{h}\right)^{0.8544} + 0.236}{\left(\frac{W}{h}\right)^{0.8544} + 0.87} \quad (5.9)$$

$$\xi_2 = 1 + \frac{\left(\frac{W}{h}\right)^{0.371}}{2.358\varepsilon_r + 1} \quad (5.10)$$

$$\xi_3 = 1 + \frac{0.5274 \arctan(0.084 \left(\frac{W}{h}\right)^{0.371})}{\varepsilon_{ref}^{0.9236}} \quad (5.11)$$

$$\xi_4 = 1 + 0.0377 \arctan(0.067 \left(\frac{W}{h}\right)^{1.456})(6 - 5\exp(0.036(1 - \varepsilon_r))) \quad (5.12)$$

$$\xi_5 = 1 - 0.218\exp(-\frac{7.5W}{h}) \quad (5.13)$$

To determine dimensions of the antenna we have to know the property of the substrate as well as properties of the media. The Rogers TMM10 electrodeposited copper foil 17μm[6] was selected for the model because it has $\varepsilon_r = 9.2$ – which is very close to the supposed propagation media - fatty tissue (Duck, 1990; C. Gabriel et al., 1996; S. Gabriel et al., 1996a, 1996b). Using media and substrate with the same properties gives the possibility to decrease the amount variables in the model to approximately 4:1 and calculation time to 16:1. Moreover, the number of variables is restricted in the modelling tool used and without the above mentioned condition, modelling is provided on the cutting edge of the tool's ability.

To be looking ahead there is another reason to use media and substrate with the same properties. That is to avoid a surface wave which will be especially obstructive to the development of array on a large size PCB.

[6] *TMM® Thermoset Microwave Laminates* (2008, 30.09.2009). Retrieved 30.03.2009, 2009, from http://www.rogerscorp.com/documents/728/acm/TMM-Thermoset-laminate-data-sheet-TMM3-TMM4-TMM6-TMM10-TMM10i.aspx

Now we can evaluate the wavelength for the selected frequency $f = 4.95GHz$, taking into account the relative permittivity of the media $\varepsilon_r = 9.2$ where our signal is travelling.

$$\lambda = \frac{c}{f\sqrt{\varepsilon_r \mu_r}} = 19.96mm \tag{5.14}$$

The last variable is required to derive initial dimensions of the developed patch antenna substrate thickness. Due to the requirement of high selectivity and narrow frequency bandwidth determined earlier, substrate with thickness 0.508 mm was selected from the range of substrates available from the manufacturer[7].

Equations (5.9) , (5.10) , (5.11) , (5.12) have been developed by (Kirschning et al., 1981) for the patch antenna working in air or a vacuum and have to take into account relative permittivity of substrate. In our case it is possible to simplify these equations due to the implied equity of the relative permittivity of the substrate and surrounding media. In simplified form:

$$\xi_1 = 0.434907 \frac{1 + 0.26}{1 + 0.189} \frac{\left(\frac{W}{h}\right)^{0.8544} + 0.236}{\left(\frac{W}{h}\right)^{0.8544} + 0.87} \tag{5.15}$$

$$\xi_2 = 1 + \frac{\left(\frac{W}{h}\right)^{0.371}}{3.358} \tag{5.16}$$

$$\xi_3 = 1 + 0.5274 \arctan\left(0.084 \left(\frac{w}{h}\right)^{0.371}\right) \tag{5.17}$$

$$\xi_4 = 1 + 0.0377 \arctan\left(0.067 \left(\frac{w}{h}\right)^{1.456}\right) \tag{5.18}$$

[7] *TMM® Thermoset Microwave Laminates* (2008, 30.09.2009). Retrieved 30.03.2009, 2009, from http://www.rogerscorp.com/documents/728/acm/TMM-Thermoset-laminate-data-sheet-TMM3-TMM4-TMM6-TMM10-TMM10i.aspx

Dimensions of the patch *L* and *W* shown in Figure 5.9 were obtained by the iterative decision of the equations (5.8), (5.6) and (5.7) for target middle frequency 4.95GHz and propagation media with $\varepsilon_r = 9.2$. The coordinates of feeding point p_L and p_W have been determined as a point on the diagonal of the patch on the middle between the centre of patch and a corner. The size of the feeding point *d* has been selected in accordance with the diameter of the central cord of the feeding cable RG405[8]. External dimensions of the patch *A* are taken as reasonable in relation to patch size.

Initial dimensions for model are represented in Table 5.1.

Table 5.1. Initial dimensions for patch antenna

L	9.26mm
W	8.844mm
p_L	2.565mm
p_W	2.461mm
d	0.508mm

5.4.2 **Establishing of the model**

In order to perform optimization an antenna element mathematical model needs to be established. The first step to establish model of patch antenna is to create a 2-D mesh on the base of the given dimensions. It is done with the aid of the PDE toolbox for MATLAB (*Partial Differential Equation Toolbox* 2009) as shown in Figure 5.1. The next step is to create a 3-D model of antenna. The MAT includes a 3-D built-in interactive mesh generator "struct3d" integrated into a MATLAB GUI. The mesh generator creates, modifies, and saves a metal/dielectric antenna mesh including the

[8] Cable,microwave,copper,1m,RG405. (2009). Retrieved 30.01.2009, 2009, from http://newzealand.rs-online.com/web/search/searchBrowseAction.html?method=searchProducts&searchTerm=388704

feeding elements. An inhomogeneous lossy dielectric material may be defined as well as metal surfaces of arbitrary planar or cylindrical shape. This mesh generator is used for any antenna/resonator type (Makarov & Kempel, 2005). Figure 5.11 shows the top side of the 3-D model for patch antenna by the mesh generator “struct3d”.

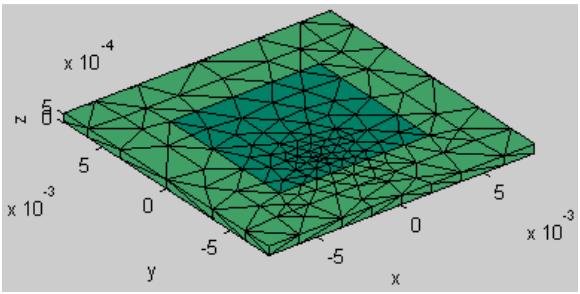

Figure 5.11 Example of 3-D model for patch antenna. All dimensions are shown in m.

The next step is to create Rao-Wilton-Glisson metal basis functions for the Method of Moments (Rao et al., 1982), the dielectric edge basis functions (De Carvalho & De Souza Mendes, 1999; Kulkarni et al., 2004), and the associated geometry parameters with built-in MAT script “wrapper.m”. This script defines all the parameters of the dielectric tetrahedral and the metal triangular mesh. After completing this step, one can evaluate the number of variables involved in the next step Method of Moments solution.

The multipoint Method of Moments solution is performed on every point of previously determined frequency band. Results for the complex input impedance are derived for the first model with dimensions from Table 5.1, are represented in Figure 5.12.

5.4.3 **Optimization**

The goals of optimization process were:

- to achieve minimal reflections on the middle frequency 4.95 GHz;
- to get two apparent resonance frequencies with Δf and Q_t determined in the section 4.2

There are two peaks apparently visible in Figure 5.12 pointed by vertical arrows *fr(L)* an *fr(W)* related to effective dimensions of the patch L_e and W_e correspondingly. The middle frequency is lower than desirable. One can see the difference between impedances for these two frequencies which leads to a narrowing of the circularly polarization zone due to the broken condition of the orthogonal components equity.

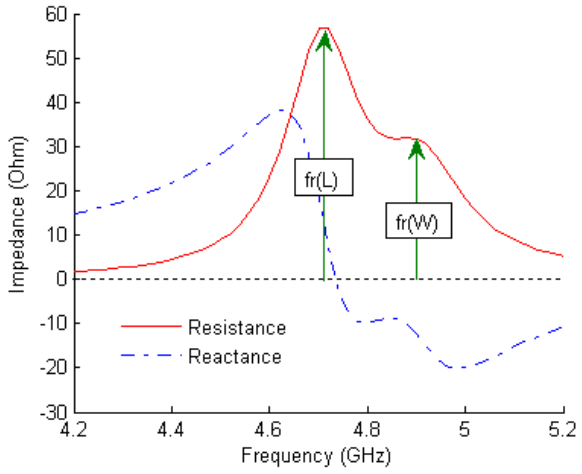

Figure 5.12 Modelled parameters for initial dimensions given in Table 5.1. Two resonance picks pointed by arrows *fr(L)* an *fr(W)* related to effective dimensions of the patch L_e and W_e correspondently. Middle frequency is around 4.8GHz

Multiple iterations with dimensions of the patch and feeding point placement have to be performed to acquire desirable middle frequency 4.95GHz equal active impedance R_{in}*=50Ohm* for both resonance frequencies, as shown in Figure 5.13.

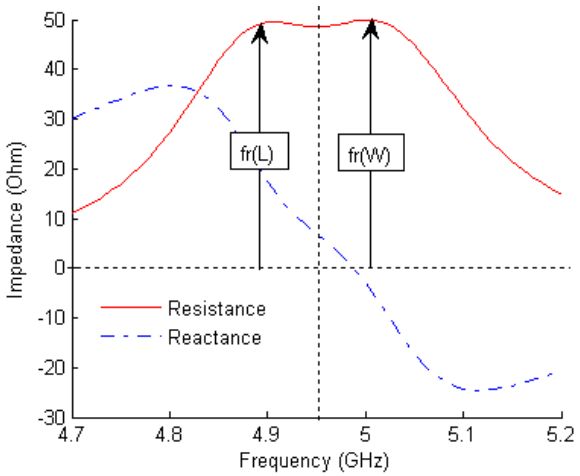

Figure 5.13 Final results of mathematical modelling. Active impedance R_{in}=*50Ohm* equal for both resonance frequencies

The final results of mathematical modelling for Reflection coefficient provided by Matlab are presented in Figure 5.14.

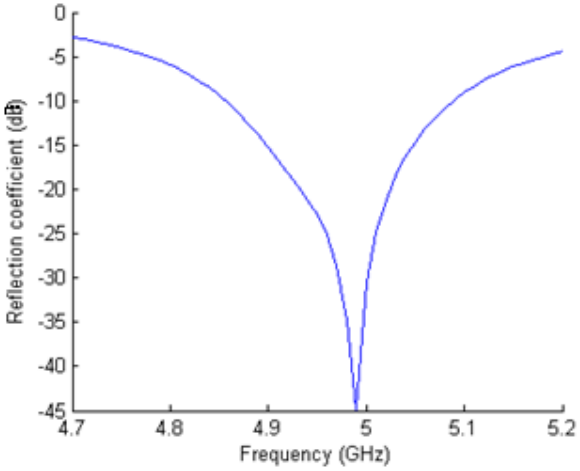

Figure 5.14 Final results of mathematical modelling. Reflection coefficient below -20dB

Dimensions derived during optimization process represented in Table 5.2.

Table 5.2. Final dimensions for the patch antenna model.

L	9mm
W	8.6mm
p_L	3.55mm
p_W	1.53mm
d	0.508mm

5.5 Summary

It is possible to improve the mathematical model particularly to place the negative pick of the reflection coefficient at 4.95GHz strictly between the resonance frequencies and minimize the value of the reactance between resonance frequencies by playing with the thickness of the patch and other dimensions, but at the later stage of the project. Moreover, at this stage it became obvious that the positioning of the feeding point will be an issue on the manufacturing stage of the real antenna element because it required the accuracy to be better than 0.001 mm to get reflection coefficient below -20dB and perfectly placed symmetric picks for both resonance frequencies of developed antenna element. Model parameters shown in Table 5.2 are sufficient to move to the next step - experiments on real antenna elements.

Chapter 6 - Results

The current work encompasses mathematical modelling, antenna setup design, design and manufacturing of antenna elements, and the measurement on the preliminary model of the antenna setup.

6.1 Antenna element

Antenna elements shown in Figure 6.7 were produced from the TMM10 substrate with a thickness 0.508mm in accordance to the dimensions given in Table 5.2. The outer sheath of the cable RG405 is soldered to the ground plane of the patch antenna and the central wire is soldered to the patch. SMA connectors[9] were soldered to the opposite end of the cable.'

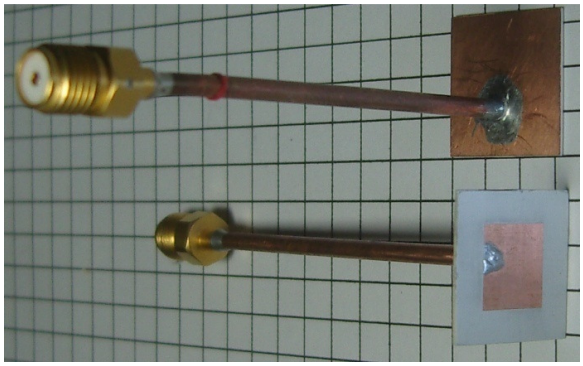

Figure 6.1 Antennas used in measurements. Dimension of the grid cell is 5x5 mm.

As mentioned above, proper selection of media is vital for the antenna setup. In our case we have made the decision to select appropriate media with $\varepsilon_r = 9.2$.

6.2 Media

To select the appropriate media with $\varepsilon_r = 9.2$ suitable for the measurement with existed budget constraints a range of materials have been considered. The antenna setup is supposed to be in contact with human skin thus it has to be chemically inactive, and physically rigid. From

[9] Connector,coaxial,RF,SMA,solder,jack,cable,50 Ohm,RG405/U. Retrieved 30.06.2009, 2009, from http://newzealand.rs-online.com/web/search/searchBrowseAction.html?method=getProduct&R=4683205

the other side, we have to evaluate a coupling between antenna elements. Thus, during measurement stage, distance between antenna elements has to vary. Therefore the media has to be non-rigid. Appropriate media can be obtained by mixing the Barium Titanate powder and two component silicone rubber RHODORSIL® RTV-585[10] as suggested by (Cherney, 2005).

The silicone rubber can be both, non-rigid on the measurement stage and rigid after curing. It is also chemically inactive. The issue is relative permittivity $\varepsilon_r = 9.2$ required in this project. The silicone rubber itself has relative permittivity $\varepsilon_r = 3$. Barium Titanate has relative permittivity $\varepsilon_r \geq 1250$. Thus mixing silicone rubber with Barium Titanate in proper proportion would give required $\varepsilon_r = 9.2$.

It is possible to add the Barium Titanate powder gradually to the compound mix and to provide intermediate measurements in order to achieve the desired relative permittivity. All processes have been done in the chemistry laboratory during several days because of the high viscosity of the final compound and encountered difficulties achieving a homogenous mix. The approximate ratio of components required to achieve relative permittivity $\varepsilon_r = 9.2$ according to (Cherney, 2005) 27% of the Barium Titanate and 73% of the RHODORSIL® RTV-585 in the volume.

While the compound mix stays soft it is possible to move and replace antenna elements during measurements. All measurements were completed without curing the silicone rubber.

After measurement and/or proper positioning antenna elements within array, silicone rubber has to be cured. This required only 2% of the catalyst 60R from the RHODORSIL® RTV-585. Such small amount would not imply any sensitive deviation in the permittivity of the cured media.

Equipment used in the media production process is shown in Figure 6.2.

[10] RHODORSIL® RTV-585. (1998). Retrieved 30.09.2009, 2009, from http://www.precisionconverting.com/downloads/rhodia_techdata/pi585.pdf

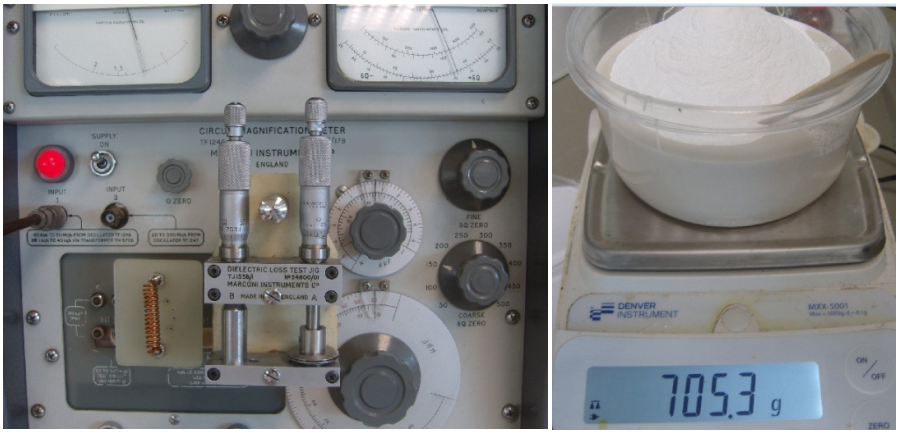

Figure 6.2 Equipment used in the media production process.

6.3 Measurements

A Vector network analyser Agilent Technologies N5230A was used to measure impedances, the reflection coefficient and phase variations. Measurements have been done for single antenna element emerged in the media and for two antenna elements as it is shown in Figure 6.3.

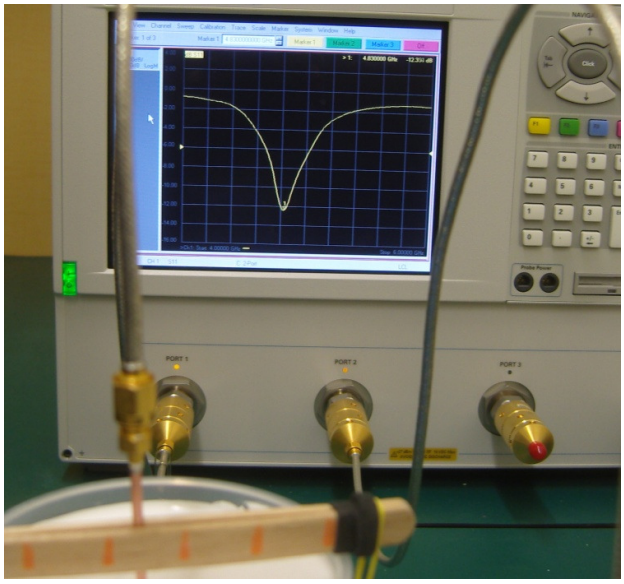

Figure 6.3 Measurement of the reflection coefficient with two antennas submerged in the media with $\varepsilon_r = 9.2$

The network analyser was calibrated for two data acquisition channels. The results of measuring impedances for single antenna element are shown in Figure 6.4.

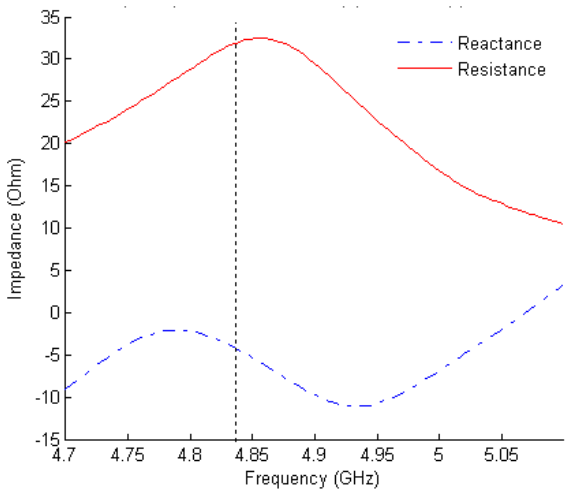

Figure 6.4 The results of measuring impedances for single antenna element. Resistance and Reactance components of the Impedance. Middle frequency shown by the vertical line is 4.84GHz

The results acquired for Reflection coefficient or S11 with the same antenna element are shown in Figure 6.5.

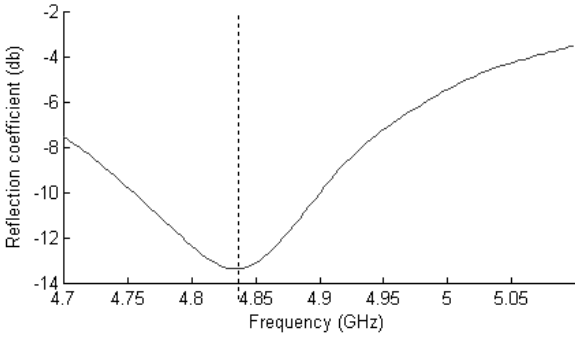

Figure 6.5 Reflection coefficient. Middle frequency is shown by the vertical line is 4.84GHz

The results for Phase variations are shown in Figure 6.6.

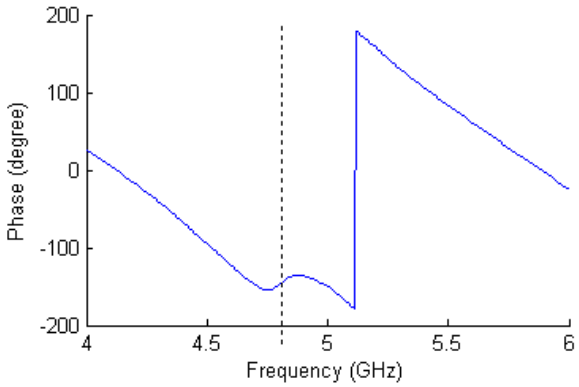

Figure 6.6 Measured phase variations. Middle frequency 4.84GHz is shown by the vertical line

Multiple measurements of the impedances for the antenna element were taken, with the second antenna element placed at different distances from the measured antenna element as shown in Figure 6.7.

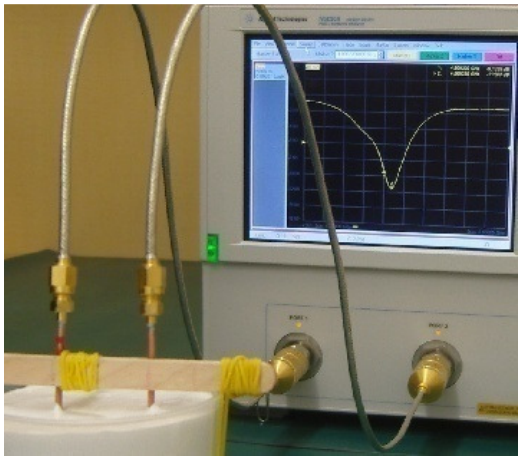

Figure 6.7 Measuring of the mutual input impedance of the antenna array. Dependency upon relative placement of antenna elements.

These measurements were taken to investigate the degree of coupling between two antenna elements. Results acquired for multiple distances between antenna elements from 16mm to 46mm with step 1mm are presented in Figure 6.8.

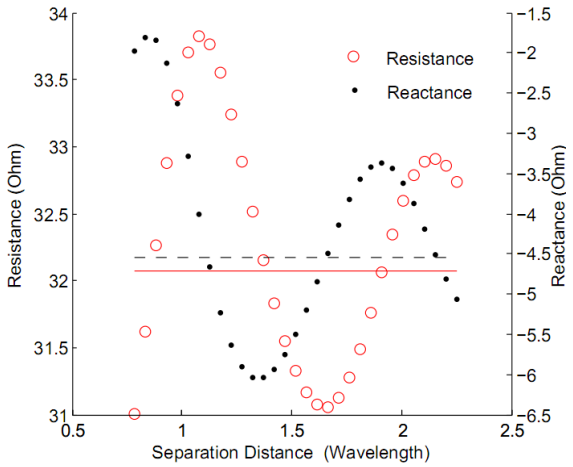

Figure 6.8 Coupling. Dependence of the Real and Imaginary parts of the mutual impedance from the distance between two antenna elements. Horizontal dashed line represents value for the Imaginary part for the single antenna and solid line correspondent value for the Real part.

Changes of Resistance are shown by the circles and Reactance by the dots. The horizontal dashed line represents value for the Imaginary part of the input impedance for the single antenna and solid line correspondent value for the Real part.

Chapter 7 - Discussion

7.1 Antenna element and media

The first problem for current antenna element manufacturing is accuracy and repeatability. The measured deviation between linear dimensions of the patch for 8 samples manufactured on the best available manufacturing facility was 1.4% despite the fact that all these 8 samples were placed on the one piece of PCB and manufactured simultaneously as shown in Figure 7.1.

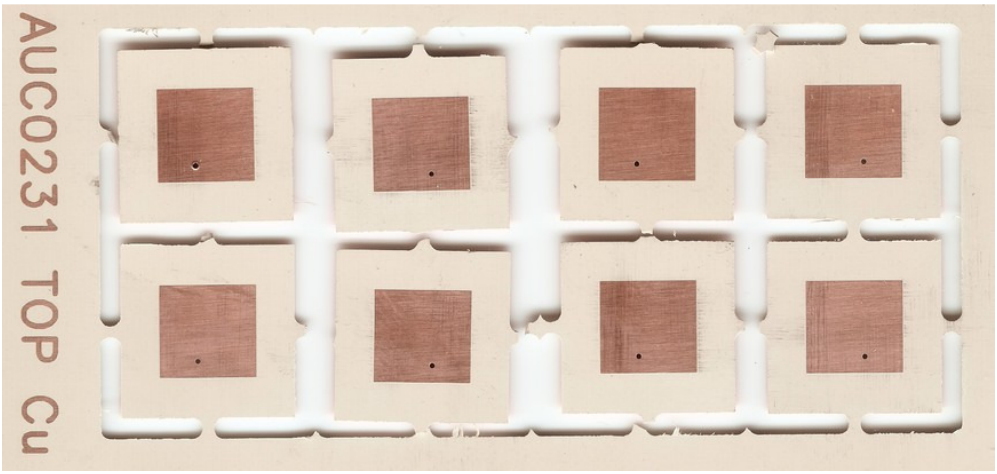

Figure 7.1 8 simultaneously manufactured antenna samples.

The second problem was the media for measurement. The approximate accuracy of the equipment shown in Figure 6.2 for the preparation of the media with related permittivity $\varepsilon_r = 9.2$ was around 5-10%.

As it could be expected the resulted properties of antenna are somewhat different to those obtained from modelling. However they are within the required for the developing system. Middle frequency shown by the vertical line Figure 6.4 is 4.84GHz which gives a 2% difference from modelled results shown in Figure 5.13. It is possible that deviations from the modelling results are partially on account of the inaccuracy of the relative permittivity media mentioned in the previous paragraph. The same reason could lead to the relatively poor reflection coefficient shown in

Figure 6.5 in comparison with those achieved from mathematical modelling shown in Figure 5.14.

The results for Phase variations are shown in Figure 6.6. Special interest is represented by phase shift around middle frequency. This shift reveals presence of two resonant frequencies in the developed patch antenna. These frequencies correspond to two orthogonal dimensions of the patch. They are close enough to introduce phase shift between orthogonal currents in the patch. The orthogonal currents with phase shift of 90^0 correspond to circularly polarised wave as explained in the Chapter 4.

7.2 Mutual coupling of two Antenna elements

As mentioned above, coupling between antenna elements will determine minimal distances between antenna elements in the array and lower spatial frequencies available for image reconstruction. Thus we should also consider the problem with coupling between antenna elements in the array.

As it has been said, that mutual coupling is the result of an undesirable energy transfer between neighbour antenna elements. Therefore, coupling leads to measurable changes in the antenna parameters. Measurements of the impedances for the same antenna element on the resonant frequency 4.84GHz have been done while the second antenna element was placed at a different distance from the measured antenna element and both elements exited. Results for Real and Imaginary parts of the impedance are shown in Figure 6.8. The horizontal dashed line represents the value for the Imaginary part for the single antenna and solid line correspondent value for the Real part. By recalculating the phase deviation from the collected data we can derive dependency for possible error value as shown in Figure 7.2.

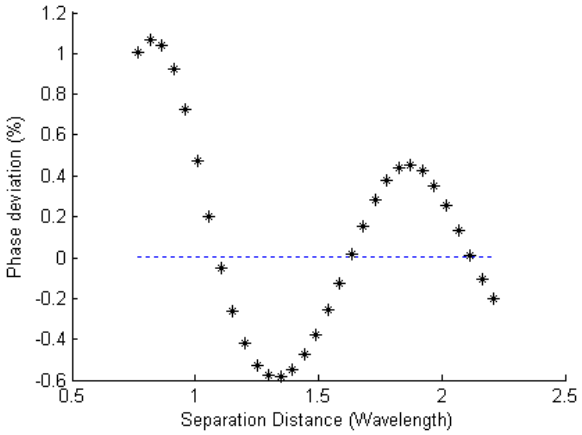

Figure 7.2 Dependency for possible error value in the phase measurements due to mutual coupling from the distance between two antenna elements.

7.3 Future Work

There are still many questions to be answered for the future implementation of proposed holography technique. We will mention here only problems related to the antenna setup.

As mentioned above there are two possible ways to improve the linear resolution of the data acquisition system. First is to reduce the distance from the antenna array to the object under investigation. However there are limitations related to wide angular deflections due to the model of microwave propagation and unavoidable refraction in the skin layer. In more detail these limitations were discussed in the sections 3.4, 3.5 and 3.6. The second way is to increase middle frequency of data acquisition system. However challenges of identical and accurate manufacturing need to be carefully considered as discussed in Chapter 7. Connecting the feed as it's been done in this work also may not be feasible as the size of antenna element reduces with the increased frequency. The feeding point needs to be properly modelled for higher frequencies. It can be achieved by using more sophisticated modelling software.

While the materials used in this work to make the propagation media between the array and the object under the test are suitable for the initial stage of the antenna setup development and inexpensive, it might be

difficult to make homogenous compound in large quantities. The combination of a suitable mixer and vacuum pump can be used. Also specially designed materials with stable dielectric properties e.g. ECCOSTOCK NiK powder [11] to allow the antenna elements to be repositioned in the media can be used, though there are expensive.

[11] *ECCOSTOCK HiK Powder*. (30.09.2009). Retrieved 30.09.2009, 2009, from http://www.eccosorb.com/products/107/ECCOSTOCK%20HiK%20Powder

Chapter 8 - Conclusions

Although the parameters of developed antenna are slightly different from one obtained in the computational model, the acceptable parameters of circular polarized patch antenna have been achieved at 4.84 GHz. Thus the methodology of modelling can be used at higher frequencies observing the accuracy of manufacturing.

Antenna setup requirements have been considered and the setup design with antenna elements submerged in media with $\varepsilon_r = 9$ has been suggested. Suggested antenna setup design should minimise issues related to changing direction of the wave front propagation and subsequent beam shift as shown in Figure 3.13. Moreover selected permittivity $\varepsilon_r = 9$ of the propagation media lets to minimise reflections from the boundary of human tissue.

In order to achieve best possible resolution for imaging, distribution of antenna elements in the antenna array has been considered and Reuleaux triangle with non-uniform antenna placement configuration was selected. Differences in separations between antennas along the sides of the triangle and across the vertices create a less symmetric and much more uniform sampling pattern in Fourier space. Perturbations of the antenna locations away from a perfect Reuleaux triangle break down symmetry in the sampling pattern leading to even more uniform coverage.

Circular polarization for developing antenna element has been selected as more suitable to collect most of the electromagnetic energy crossing the antenna aperture by full use of the polarization components. This selection is aimed to increase power of the acquired signal while maintaining appropriate irradiation level.

To obtain a sufficient quality of an image, the antenna array needs to contain as many elements as possible. The area required to place the antenna elements on the array plane is determined by the size of antenna

element, its type and feeding circuitry. Selection of the near square patch as base antenna element type has allowed fulfilling this requirement.

To provide validation trials, multiple antenna elements were manufactured. The measured deviation between linear dimensions of the patch for 8 samples manufactured on the best available manufacturing facility was found 1.4%. Single and paired antenna elements have been tested using Vector Network Analyser. The found middle frequency 4.84GHz is within 2% from modelled one.

Although the antenna element requirement analysis and design discussed in this work require some additional development, this work makes a starting point for the further development of the microwave holography technique for early breast cancer detection.

In summary, the result of this work shows feasibility of selected approach for modelling, testing and manufacturing the antenna elements for breast cancer microwave imaging.

References

Andres, N., Arroyo, P., & Quintanilla, M. (1997). Velocity measurements in a convective flow by holographic interferometry. *Applied Optics, 36*(27), 6997-7007.

Arunachalam, K. (2007). *Investigation of a deformable mirror microwave imaging and therapy technique for breast cancer.* Unpublished Ph.D., Michigan State University, United States -- Michigan. http://proquest.umi.com/pqdweb?did=1354134991&Fmt=7&clientId=7961&RQT=309&VName=PQD

Balanis, C. A. (1997). *Antenna Theory Analysis and Design* (2-nd ed.). New York: WILEY-INTERSCIENCE.

Benton, S. A., & Bove, V. M. (2008). *Holographic imaging*. Hoboken, N.J.: Wiley-Interscience.

Bocquet, B., van de Velde, J. C., Mamouni, A., Leroy, Y., Giaux, G., Delannoy, J., et al. (1990). Microwave radiometric imaging at 3 GHz for the exploration of breast tumors. *IEEE Transactions on Microwave Theory and Techniques, 38*(6), 791-793.

Bolomey Ch, J., Izadnegahdar, A., & Jofre, L. (1982). Microwave diffraction tomography for biomedical applications. *IEEE Transactions on Microwave Theory and Techniques, 30*(11), 1998-2000.

Bolomey, J. C., Jofre, L., & Peronnet, G. (1983). ON THE POSSIBLE USE OF MICROWAVE-ACTIVE IMAGING FOR REMOTE THERMAL SENSING. *IEEE Transactions on Microwave Theory and Techniques, MTT-31*(9 pt 1), 777-778.

Bolomey, J. C., Pichot, C., & Garboriaud, G. (1991). Planar microwave imaging camera for biomedical applications. Critical and prospective analysis of reconstruction algorithms. *Radio Science, 26*(2), 541-549.

Bond, E. J., Li, X., Hagness, S. C., & Van Veen, B. D. (2003). Microwave imaging via space-time beamforming for early detection of breast cancer. *IEEE Transactions on Antennas and Propagation, 51*(8), 1690-1705.

Born, M., & Wolf, E. (1999). *Principles of optics : electromagnetic theory of propagation, interference and diffraction of light* (7th ed.). Cambridge: Cambridge University Press.

Borza, D. N. (1998). Specialized techniques in holographic non-destructive testing of composites. *Composites Part B: Engineering, 29*(4), 497-504.

The Breasts. (2008). from http://www.cancer.gov/cancertopics/wyntk/breast/page2

Brown, G. H., & Woodward, O. M. (1947). CIRCULARLY-POLARIZED OMNIDIRECTIONAL ANTENNA. *RCA review*.

Bulyshev, A. E., Semenov, S. Y., Souvorov, A. E., Svenson, R. H., Nazarov, A. G., Sizov, Y. E., et al. (2001). Computational modeling

of three-dimensional microwave tomography of breast cancer. *Biomedical Engineering, IEEE Transactions on, 48*(9), 1053-1056.

Caorsi, S., Ciaramella, S., Gragnani, G. L., & Pastorino, M. (1995). On the use of regularization techniques in numerical inverse-scattering solutions for microwave imaging applications. *IEEE Transactions on Microwave Theory and Techniques, 43*(3), 632-640.

Caorsi, S., Gragnani, G. L., & Pastorino, M. (1993). Reconstruction of dielectric permittivity distributions in arbitrary 2-D inhomogeneous biological bodies by a multiview microwave numerical method. *IEEE Transactions on Medical Imaging, 12*(2), 232-239.

Carr, K. L. (1989). Microwave radiometry: Its importance to the detection of cancer. *IEEE Transactions on Microwave Theory and Techniques, 37*(12), 1862-1869.

Carr, K. L. (1989). Microwave radiometry: its importance to the detection of cancer. *Microwave Theory and Techniques, IEEE Transactions on, 37*(12), 1862-1869.

Carr, K. L., Cevasco, P., Dunlea, P., & Shaeffer, J. (2000). Radiometric sensing: an adjuvant to mammography to determine breast biopsy. *IEEE MTT-S International Microwave Symposium Digest, 2*, 929-932.

Cherney, E. A. (2005). Silicone rubber dielectrics modified by inorganic fillers for outdoor high voltage insulation applications. *IEEE Transactions on Dielectrics and Electrical Insulation, 12*(6), 1108-1115.

Chunjing, T., Tao, S., Wenhui, Y., & Shizeng, W. (2006). *Ultra-wideband Microwave-Induced Thermoacoustic Tomography of Human Tissues.* Paper presented at the Nuclear Science Symposium Conference Record, 2006. IEEE.

Cole, K. S., & Cole, R. H. (1941). Dispersion and absorption in dielectrics I. Alternating current characteristics. *The Journal of Chemical Physics, 9*(4), 341-351.

Converse, M., Bond, E. J., Van Veen, B. D., & Hagness, S. C. (2006). A computational study of ultra-wideband versus narrowband microwave hyperthermia for breast cancer treatment. *IEEE Transactions on Microwave Theory and Techniques, 54*(5), 2169-2180.

Cornwell, T. J. (1988). Novel principle for optimization of the instantaneous Fourier plane coverage of correlation arrays. *IEEE Transactions on Antennas and Propagation, 36*(8), 1165-1167.

Davis, S. K. (2006). *Ultrawideband radar-based detection and classification of breast tumors.* Unpublished Ph.D., The University of Wisconsin - Madison, United States -- Wisconsin. http://proquest.umi.com/pqdweb?did=1221710141&Fmt=7&clientId=7961&RQT=309&VName=PQD

Davis, S. K., Bond, E. J., Li, X., Hagness, S. C., & Van Veen, B. D. (2003). Microwave imaging via space-time beamforming for early detection of breast cancer: Beamformer design in the frequency domain. *Journal of Electromagnetic Waves and Applications, 17*(2), 357-381.

Davis, S. K., Van Veen, B. D., Hagness, S. C., & Kelcz, F. (2008). Breast tumor characterization based on ultrawideband microwave backscatter. *IEEE Transactions on Biomedical Engineering, 55*(1), 237-246.

De Carvalho, S. A., & De Souza Mendes, L. (1999). Scattering of EM waves by inhomogeneous dielectrics with the use of the method of moments and 3-D solenoidal basis functions. *Microwave and Optical Technology Letters, 23*(1), 42-46.

Duck, F. A. (1990). *Physical properties of tissue*. London, UK: Academic Press Inc

Elmore, J. G., Barton, M. B., Moceri, V. M., Polk, S., Arena, P. J., & Fletcher, S. W. (1998). Ten-year risk of false positive screening mammograms and clinical breast examinations. *New England Journal of Medicine, 338*(16), 1089-1096.

Elsdon, M., Leach, M., Fdo, M. J., Foti, S. J., & Smith, D. (2007). *Early stage breast cancer detection using indirect microwave holography.* Paper presented at the Proceedings of the 36th European Microwave Conference, EuMC 2006, Manchester. http://www.scopus.com/scopus/inward/record.url?eid=2-s2.0-41649090053&partnerID=40

Elsdon, M., Leach, M., Skobelev, S., & Smith, D. (2006). *Microwave holographic imaging of breast cancer.* Paper presented at the IEEE 2007 International Symposium on Microwave, Antenna, Propagation and EMC Technologies for Wireless Communications, MAPE, Hangzhou. http://www.scopus.com/scopus/inward/record.url?eid=2-s2.0-47649096195&partnerID=40

Fear, E. C., Hagness, S. C., Meaney, P. M., Okoniewski, M., & Stuchly, M. A. (2002). Enhancing breast tumor detection with near-field imaging. *IEEE Microwave Magazine, 3*(1), 48-56.

Fear, E. C., Li, X., Hagness, S. C., & Stuchly, M. A. (2002). Confocal microwave imaging for breast cancer detection: Localization of tumors in three dimensions. *IEEE Transactions on Biomedical Engineering, 49*(8), 812-822.

Fear, E. C., Meaney, P. M., & Stuchly, M. A. (2003). Microwaves for breast cancer detection? *Potentials, IEEE, 22*(1), 12-18.

Fear, E. C., Sill, J., & Stuchly, M. A. (2003). Experimental feasibility study of confocal microwave imaging for breast tumor detection. *Microwave Theory and Techniques, IEEE Transactions on, 51*(3), 887-892.

Fear, E. C., & Stuchly, M. A. (2000). Microwave detection of breast cancer. *Microwave Theory and Techniques, IEEE Transactions on, 48*(11), 1854-1863.

Foster, K. R., & Schwan, H. P. (1989). Dielectric properties of tissues and biological materials: a critical review. *Critical Reviews in Biomedical Engineering, 17*(1), 25-104.

Foster, K. R., & Schwan, H. P. (1996). *Dielectric properties of tissues*. Boca Raton: CRC Press.

Franchois, A., Joisel, A., Pichot, C., & Bolomey, J. C. (1998). Quantitative microwave imaging with a 2.45-GHz planar microwave camera. *IEEE Transactions on Medical Imaging, 17*(4), 550-561.

Franchois, A., & Pichot, C. (1997). Microwave imaging-complex permittivity reconstruction with a levenberg-marquardt method. *IEEE Transactions on Antennas and Propagation, 45*(2), 203-215.

Franza, O., Joachimowicz, N., & Bolomey, J. C. (2002). SICS: A sensor interaction compensation scheme for microwave imaging. *IEEE Transactions on Antennas and Propagation, 50*(2), 211-216.

Gabor, D. (1948). A new microscopic principle. *Nature, 161*(4098), 777-778.

Gabriel, C., Gabriel, S., & Corthout, E. (1996). The dielectric properties of biological tissues: I. Literature survey. *Physics in Medicine and Biology, 41*(11), 2231-2249.

Gabriel, C., Grant, E. H., & Young, I. R. (1986). Use of time domain spectroscopy for measuring dielectric properties with a coaxial probe. *Journal of Physics E: Scientific Instruments, 19*(10), 843-846.

Gabriel, C., & Peyman, A. (2006). Dielectric measurement: Error analysis and assessment of uncertainty. *Physics in Medicine and Biology, 51*(23), 6033-6046.

Gabriel, S., Lau, R. W., & Gabriel, C. (1996a). The dielectric properties of biological tissues: II. Measurements in the frequency range 10 Hz to 20 GHz. *Physics in Medicine and Biology, 41*(11), 2251-2269.

Gabriel, S., Lau, R. W., & Gabriel, C. (1996b). The dielectric properties of biological tissues: III. Parametric models for the dielectric spectrum of tissues. *Physics in Medicine and Biology, 41*(11), 2271-2293.

Hagness, S. C., Taflove, A., & Bridges, J. E. (1998a). Two-dimensional FDTD analysis of a pulsed microwave confocal system for breast cancer detection: Fixed-focus and antenna-array sensors. *IEEE Transactions on Biomedical Engineering, 45*(12), 1470-1479.

Hagness, S. C., Taflove, A., & Bridges, J. E. (1998b). Two-dimensional FDTD analysis of a pulsed microwave confocal system for breast cancer detection: fixed-focus and antenna-array sensors. *Biomedical Engineering, IEEE Transactions on, 45*(12), 1470-1479.

Hagness, S. C., Taflove, A., & Bridges, J. E. (1999). Three-dimensional FDTD analysis of a pulsed microwave confocal system for breast cancer detection: design of an antenna-array element. *Antennas and Propagation, IEEE Transactions on, 47*(5), 783-791.

Hartov, A., Mazzarese, R. A., Reiss, F. R., Kerner, T. E., Osterman, K. S., Williams, D. B., et al. (2000). A multichannel continuously selectable multifrequency electrical impedance spectroscopy measurement system. *IEEE Transactions on Biomedical Engineering, 47*(1), 49-58.

Hassan, R., Cohanim, B., De Weck, O., & Venter, G. (2005). *A comparison of particle swarm optimization and the genetic algorithm.* Paper presented at the Collection of Technical Papers - AIAA/ASME/ASCE/AHS/ASC Structures, Structural Dynamics and Materials Conference, Austin, TX.

http://www.scopus.com/inward/record.url?eid=2-s2.0-28844454271&partnerID=40
Hayt, W. H., & Buck, J. A. (2001). *Engineering Electromagnetics* (6-th ed.). New York: McGraw-Hill.
Hermann, L. (1872). Ueber eine Wirkung galvanischer StrΓ¶me auf Muskeln und Nerven. *PflΓger, Archiv fΓr die Gesammte Physiologie des Menschen und der Thiere, 5*(1), 223-275.
Huang, J. (1986). A technique for an array to generate circular polarization with linearly polarized elements. *Antennas and Propagation, IEEE Transactions on, 34*(9), 1113-1124.
Huynh, P. T., Jarolimek, A. M., & Daye, S. (1998). The False-negative Mammogram. *Radiographics, 18*(5), 1137-1154.
Jin, N., & Rahmat-Samii, Y. (2008). Analysis and particle swarm optimization of correlator antenna arrays for radio astronomy applications. *IEEE Transactions on Antennas and Propagation, 56*(5), 1269-1279.
Jofre, L., Hawley, M. S., Broquetas, A., De Los Reyes, E., Ferrando, M., & Elias-Fuste, A. R. (1990). Medical imaging with a microwave tomographic scanner. *IEEE Transactions on Biomedical Engineering, 37*(3), 303-312.
Johnson, C. C., & Guy, A. W. (1972). Nonionizing electromagnetic wave effects in biological materials and systems. *Proceedings of the IEEE, 60*(6), 692-718.
Keto, E. (1997). The Shapes of Cross-Correlation Interferometers. *The Astrophysical Journal*.
Kirschning, M., Jansen, R. H., & Koster, N. H. L. (1981). ACCURATE MODEL FOR OPEN END EFFECT OF MICROSTRIP LINES. *Electronics Letters, 17*(3), 123-125.
Kruger, R. A., Kopecky, K. K., Aisen, A. M., Reinecke, D. R., Kruger, G. A., & Kiser Jr, W. L. (1999). Thermoacoustic CT with radio waves: A medical imaging paradigm. *Radiology, 211*(1), 275-278.
Kruger, R. A., Stantz, K., & Kiser Jr, W. L. (2002). *Thermoacoustic CT of the breast.* Paper presented at the Proceedings of SPIE - The International Society for Optical Engineering, San Diego, CA. http://www.scopus.com/scopus/inward/record.url?eid=2-s2.0-0036033582&partnerID=40&rel=R8.0.0
Kulkarni, S., Lemdiasov, R., Ludwig, R., & Makarov, S. (2004). Comparison of two sets of low-order basis functions for tetrahedral VIE modeling. *IEEE Transactions on Antennas and Propagation, 52*(10), 2789-2794.
Kurosaki, Y., & Kashiwagi, T. (1990). Visualization of thermal behavior of fluid by laser holographic interferometry. *Experimental Thermal and Fluid Science, 3*(1), 87-107.
Lazebnik, M., McCartney, L., Popovic, D., Watkins, C. B., Lindstrom, M. J., Harter, J., et al. (2007). A large-scale study of the ultrawideband microwave dielectric properties of normal breast tissue obtained from reduction surgeries. *Physics in Medicine and Biology, 52*(10).
Lee, S. J., & Kim, S. (2004). Application of holographic interferometry and 2D PIV for HSC convective flow diagnostics. *Measurement Science and Technology, 15*(4), 664-672.

Li, X., Bond, E. J., Hagness, S. C., Van Veen, B. D., & Van der Weide, D. (2002). Three-dimensional microwave imaging via space-time beamforming for breast cancer detection. *IEEE AP-S International Symposium and USNC/URSI Radio Science Meeting*.

Li, X., Davis, S. K., Hagness, S. C., Van Der Weide, D. W., & Van Veen, B. D. (2004). Microwave imaging via space-time beamforming: Experimental investigation of tumor detection in multilayer breast phantoms. *IEEE Transactions on Microwave Theory and Techniques, 52*(8 II), 1856-1865.

Liu, Q. H., Zhang, Z. Q., Wang, T. T., Bryan, J. A., Ybarra, G. A., Nolte, L. W., et al. (2002). Active microwave imaging I - 2-D forward and inverse scattering methods. *IEEE Transactions on Microwave Theory and Techniques, 50*(1), 123-133.

Makarov, S. N. (2002). *Antenna and EM Modeling with MATLAB*: WILEY-INTERSCIENCE.

Makarov, S. N., & Kempel, L. C. (2005, 2005). *MATLAB Antenna Toolbox. A draft*. Retrieved 10.10.2008, 2008, from http://ece.wpi.edu/mom/

Matsumoto, T., Watanabe, T., & Kojima, A. (2007). *Deformation analysis of the human femur by holographic interferometry.* Paper presented at the Annual International Conference of the IEEE Engineering in Medicine and Biology - Proceedings, Lyon. http://www.scopus.com/inward/record.url?eid=2-s2.0-57649177682&partnerID=40

Meaney, P. M., Fanning, M. W., Dun, L., Poplack, S. P., & Paulsen, K. D. (2000). A clinical prototype for active microwave imaging of the breast. *Microwave Theory and Techniques, IEEE Transactions on, 48*(11), 1841-1853.

Meaney, P. M., Paulsen, K. D., & Chang, J. T. (1998). Near-field microwave imaging of biologically-based materials using a monopole transceiver system. *IEEE Transactions on Microwave Theory and Techniques, 46*(1), 31-45.

Meaney, P. M., Paulsen, K. D., Chang, J. T., Fanning, M. W., & Hartov, A. (1999). Nonactive antenna compensation for fixed-array microwave imaging. II. Imaging results. *Medical Imaging, IEEE Transactions on, 18*(6), 508-518.

Meaney, P. M., Paulsen, K. D., Hartov, A., & Crane, R. K. (1995). An active microwave imaging system for reconstruction of 2-D electrical property distributions. *Biomedical Engineering, IEEE Transactions on, 42*(10), 1017-1026.

Meaney, P. M., Paulsen, K. D., & Ryan, T. P. (1995). Two-dimensional hybrid element image reconstruction for TM illumination. *IEEE Transactions on Antennas and Propagation, 43*(3), 239-247.

Miyakawa, M. (1993). Tomographic measurement of temperature change in phantoms of the human body by chirp radar-type microwave computed tomography. *Medical and Biological Engineering and Computing, 31*(4 SUPPL.).

Moore, S. K. (2001). Better breast cancer detection. *IEEE Spectrum, 38*(5), 50-54.

Nunes, F. L. S., & Schiabel, H. (2000). *Contrast enhancement procedure for digital images of dense breasts by using tissue attenuation*

coefficients. Paper presented at the Engineering in Medicine and Biology Society, 2000. Proceedings of the 22nd Annual International Conference of the IEEE.

NZ Breast Cancer Facts (2008). Retrieved 12.03.2009, 2009, from http://www.nzbcf.org.nz/breastcancer/facts_in_nz.asp

Partial Differential Equation Toolbox (2009). Retrieved 1.10.2009, 2009

Rao, S. M., Wilton, D. R., & Glisson, A. W. (1982). ELECTROMAGNETIC SCATTERING BY SURFACES OF ARBITRARY SHAPE. *IEEE Transactions on Antennas and Propagation, AP-30*(3), 409-418.

Ruf, C. S. (1993). Numerical annealing of low-redundancy linear arrays. *IEEE Transactions on Antennas and Propagation, 41*(1), 85-90.

Ryle, M., & Vonberg, D. D. (1946). Solar radiation on 175Mc/s. *Nature, 158* (September 1946), 339.

Semenov, S. Y., Bulyshev, A. E., Abubakar, A., Posukh, V. G., Sizov, Y. E., Souvorov, A. E., et al. (2005). Microwave-tomographic imaging of the high dielectric-contrast objects using different image-reconstruction approaches. *IEEE Transactions on Microwave Theory and Techniques, 53*(7), 2284-2293.

Semenov, S. Y., Svenson, R. H., Boulyshev, A. E., Souvorov, A. E., Borisov, V. Y., Sizov, Y., et al. (1996). Microwave tomography: Two-dimensional system for biological imaging. *IEEE Transactions on Biomedical Engineering, 43*(9), 869-877.

Semenov, S. Y., Svenson, R. H., Bulyshev, A. E., Souvorov, A. E., Nazarov, A. G., Sizov, Y. E., et al. (2002). Three-dimensional microwave tomography: Initial experimental imaging of animals. *IEEE Transactions on Biomedical Engineering, 49*(1), 55-63.

Semouchkina, E., Semouchkin, G., Lanagan, M., Ivanchenko, I., Koroljev, S., & Popenko, N. (2004). *A new approach for enhancement circular polarization output in square shaped microstrip patch antennas.* Paper presented at the IEEE Antennas and Propagation Society, AP-S International Symposium (Digest), Monterey, CA. http://www.scopus.com/scopus/inward/record.url?eid=2-s2.0-4544366083&partnerID=40

Sergieiev, O., & Kitaev, V. (2009). *Circular Polarised Patch Antenna for Medical Microwave Holography.* Paper presented at the ENZCon 2009, University of Otago, Dunedin, New Zealand

Sill, J. M., & Fear, E. C. (2005). Tissue sensing adaptive radar for breast cancer detection-experimental investigation of simple tumor models. *IEEE Transactions on Microwave Theory and Techniques, 53*(11), 3312-3319.

Smith, D., Leach, M., & Sambell, A. (2002). *An indirect holographic method for determining antenna radiation patterns and imaging antenna fields.* Paper presented at the Antennas and Propagation Society International Symposium, 2002. IEEE.

Souvorov, A. E., Bulyshev, A. E., Semenov, S. Y., Svenson, R. H., & Tatsis, G. P. (2000). Two-dimensional computer analysis of a microwave flat antenna array for breast cancer tomography. *IEEE Transactions on Microwave Theory and Techniques, 48*(8), 1413-1415.

Stutzman, W. L., & Thiele, G. A. (1997). *Antenna Theory and Design* (2-nd ed.): John Wiley and Sons.

Swicord, M., & Balzano, Q. (2008). Has Electromagnetic Energy in the Band 0.1–100 GHz Useful Medical Applications? A Review of Mechanisms and Biological Database Offers Dim Prospects. *Plasma Science, IEEE Transactions on, 36*(4), 1638-1649.

Taniguchi, M., & Takagi, T. (1994). Holographic pattern measuring system and its application to deformation analysis of printed circuit board due to heat of mounted parts. *IEEE Transactions on Instrumentation and Measurement, 43*(2), 326-331.

Tao, C., Song, T., Yang, W., & Wu, S. (2007). *Ultra-wideband microwave-induced thermoacoustic tomography of human tissues.* Paper presented at the IEEE Nuclear Science Symposium Conference Record, San Diego, CA. http://www.scopus.com/scopus/inward/record.url?eid=2-s2.0-38649088265&partnerID=40&rel=R7.0.0

Thompson, R., Moran,J, Swenson,G. (2007). *Interferometry and Synthesis in Radio Astronomy* (2nd ed.): Wiley:.

Tricoles, G., & Farhat, N. H. (1977). Microwave holography: Applications and techniques. *Proceedings of the IEEE, 65*(1), 108-121.

Vincitorio, F., Ramil, A., Lopez, A. J., Saavedra, E., & Yanez, A. (2008). *NDT testing by holographic interferometry applied to the structural diagnostic of artwork conservations by means of sound wave excitation.* Paper presented at the Proceedings of SPIE - The International Society for Optical Engineering, Ancona.

Wagner, K. W. (1914). Erklärung der dielektrischen Nachwirkungsvorgänge auf Grund Maxwellscher Vorstellungen. *Electrical Engineering (Archiv fur Elektrotechnik), 2*(9), 371-387.

Wang, L. V., Zhao, X., Sun, H., & Ku, G. (1999). Microwave-induced acoustic imaging of biological tissues. *Review of Scientific Instruments, 70*(9), 3744-3748.

Wendie, A. B., Jeffrey, D. B., Jean, B. C., Ellen, B. M., Daniel, L., Marcela, B.-V., et al. (2008). Combined Screening With Ultrasound and Mammography vs Mammography Alone in Women at Elevated Risk of Breast Cancer. *JAMA, 299*(18), 2151.

Winters, D. W., Shea, J. D., Madsen, E. L., Frank, G. R., Van Veen, B. D., & Hagness, S. C. (2008). Estimating the Breast Surface Using UWB Microwave Monostatic Backscatter Measurements. *Biomedical Engineering, IEEE Transactions on, 55*(1), 247-256.

X-ray danger: get the big picture. Your cumulative radiation dose is growing. Do you really need to add to it? (2006). *Heart advisor / the Cleveland Clinic, 9*(12), 3.

Xi, Z., Houjun, S., Jiwei, H., & Xin, L. (2008). *Design of an array configuration for 2-D synthetic aperture radiometers using multi-objective optimization.* Paper presented at the Proceedings of 2008 Asia Pacific Microwave Conference, APMC 2008, Hong Kong. http://www.scopus.com/inward/record.url?eid=2-s2.0-69649095179&partnerID=40

Xu, L., & Hagness, S. C. (2001). A confocal microwave imaging algorithm for breast cancer detection. *Microwave and Wireless Components Letters, IEEE, 11*(3), 130-132.

Xu, M., & Wang, L. V. (2002). Pulsed-microwave-induced thermoacoustic tomography: Filtered backprojection in a circular measurement configuration. *Medical Physics, 29*(8), 1661-1669.

Xu, M., & Wang, L. V. (2003). Analytic explanation of spatial resolution related to bandwidth and detector aperture size in thermoacoustic or photoacoustic reconstruction. *Physical Review E - Statistical, Nonlinear, and Soft Matter Physics, 67*(5 2).

Xu, M., Xu, Y., & Wang, L. V. (2003). Time-domain reconstruction algorithms and numerical simulations for thermoacoustic tomography in various geometries. *IEEE Transactions on Biomedical Engineering, 50*(9), 1086-1099.

Xu, R. P., Huang, X. D., & Cheng, C. H. (2007). Broadband circularly polarized wide-slot antenna. *Microwave and Optical Technology Letters, 49*(5), 1005-1007.

Yun, X., Fear, E. C., & Johnston, R. H. (2005). Compact Antenna for Radar-Based Breast Cancer Detection. *Antennas and Propagation, IEEE Transactions on, 53*(8), 2374-2380.

Zhang, J., Fear, E. C., & Johnston, R. H. (2009). Cross-Vivaldi antenna for breast tumor detectlon. *Microwave and Optical Technology Letters, 51*(2), 275-280.

Zhao, G., Chen, L. N., & Jiao, Y. C. (2008). Design of a broadband dual circularly polarized square slot antenna. *Microwave and Optical Technology Letters, 50*(10), 2639-2642.

List of Abbreviations and Acronyms

Acronyms	Meaning
2-D	2-Dimention
3-D	3-Dimention
A1	Antenna 1
A2	Antenna 2
AA	Antenna Array
AC	Alternating Current
AS	Antenna Setup
COMSOL	Commercial Solutions
CP	Circularly Polarized
DC	Direct Current
GUI	Graphical User Interface
HFSS	High Frequency Structure Simulator
LCIS	Lobular Carcinoma in situ
MAT	MATLAB Antenna Toolbox
MATLAB	Matrix Laboratory
MIST	Microwave Imaging via Space–Time
MITT	Microwave-Induced Thermo acoustic Tomography
MRI	Magnetic Resonance Imaging
OUI	Object Under Investigation
PCB	Printed Circuit Board
PDE	Partial Differential Equation
PVC	Polyvinyl chloride
RA	Receiving Antenna
RF	Radio Frequency
RG	Radio Guide
RWG	Rao-Wilton-Glisson
SMA	SubMiniature version A
TA	Transmitting Antenna
TAA	Transmitting Antenna Array
TMM	Thermoset Microwave Material
UWB	Ultra Wide Band
VSWR	Voltage Standing Wave Ratio

Appendix - CD Directory Listing

This CD contains the results from the modelling and experimental results used in this thesis as well as MATLAB scripts used on final stage. The file locations are explained below.

The CD is split into two sections, MATLAB scripts and Results which are described below.

MATLAB scripts

Mesh generation

Directory: \MATLAB scripts\1_mesh

This directory contains MATLAB scripts and data files required for generation 2-D and 3-D mesh of patch antenna.

Directory: \MATLAB scripts\1_mesh\codes

This directory contains additional MATLAB codes required for proper functionality of the scripts from parent directory.

Basis functions

Directory: \MATLAB scripts\2_basis

This directory contains MATLAB scripts and data files required for generation basis functions for patch antenna model.

Directory: \MATLAB scripts\2_basis\codes

This directory contains additional MATLAB codes required for proper functionality of the scripts from parent directory.

Method of Moments

Directory: \MATLAB scripts\3_mom

This directory contains MATLAB scripts and data files required for modelling of patch antenna.

Directory: \MATLAB scripts\3_mom\codes

This directory contains additional MATLAB codes required for proper functionality of the scripts from parent directory.

Results

Experimental Results

Coupling

Directory: \Results\Experimental Results\Coupling

This directory contains pre-processed MATLAB data file of 31 separate measurements for evaluation of coupling between two antenna elements.

Figures

Directory: \Results\Experimental Results\Figures

This directory contains figures acquired during measurement data analysis.

Network Analyser

Directory: \Results\Experimental Results\Network Analyser

This directory contains row data acquired during measurement with network analyser for various experimental setup configurations.

Simulation Results

Basis functions

Directory: \Results\Simulation Results\Basis functions

This directory contains MATLAB data files with generated basis functions required for patch antenna modelling.

Figures

Directory: \Results\Simulation Results\Figures

This directory contains figures acquired during preparation and modelling of antenna elements.

Mesh generated

Directory: \Results\Simulation Results\Mesh generated

This directory contains MATLAB scripts and data files for 2-D and 3-D meshes acquired during preparation for antenna modelling.

Method of Moments Results

Directory: \Results\Simulation Results\Method of Moments Results

This directory contains MATLAB data files acquired during modelling of antenna elements.